Available online at www.sciencedirect.com
SCIENCE DIRECT®

Engineering Fracture Mechanics 71 (2004) 1907–1950

Engineering Fracture Mechanics

www.elsevier.com/locate/engfracmech

A new approach to compute T-stress in functionally graded materials by means of the interaction integral method

Glaucio H. Paulino *, Jeong-Ho Kim

Department of Civil and Environmental Engineering, University of Illinois at Urbana-Champaign, 2209 Newmark Laboratory, 205 North Mathews Avenue, Urbana, IL 61801-2352, USA

Received 4 April 2003; received in revised form 14 November 2003; accepted 24 November 2003

Abstract

A "non-equilibrium" formulation is developed for evaluating T-stress in functionally graded materials with mixed-mode cracks. The T-stress is evaluated by means of the interaction integral (conservation integral) method in conjunction with the finite element method. The gradation of material properties is integrated into the element stiffness matrix using the so-called "generalized isoparametric formulation". The types of material gradation considered include exponential, linear, and radially graded exponential functions; however, the present formulation is not limited to specific functions and can be readily extended to micromechanics models. This paper investigates several fracture problems (including both homogeneous and functionally graded materials) to verify the proposed formulation, and also provides numerical solutions to various benchmark problems. The accuracy of numerical results is discussed by comparison with available analytical, semi-analytical, or numerical solutions. The revisited interaction integral method is shown to be an accurate and robust scheme for evaluating T-stress in functionally graded materials.

Keywords: Functionally graded material (FGM); T-stress; Stress intensity factor (SIF); Finite element method (FEM); Generalized isoparametric formulation (GIF); Interaction integral; Conservation integral

1. Introduction

Functionally graded materials (FGMs) are new advanced multifunctional composites in which the volume fractions of constituent materials vary smoothly, thus giving a non-uniform microstructure with continuously graded macroproperties [1]. These materials were introduced to take advantage of ideal behavior of its constituents, e.g. heat and corrosion resistance of ceramics together with mechanical strength and toughness of metals, such as in the FGM system composed of partially stabilized zirconia (PSZ) and CrNi alloy [2]. The books by Suresh and Mortensen [3] and Miyamoto et al. [4], and the review chapter by Paulino et al. [5] present comprehensive information about various aspects of FGMs.

* Corresponding author. Tel.: +1-217-333-3817; fax: +1-217-265-8041.
E-mail address: paulino@uiuc.edu (G.H. Paulino).

0013-7944/$ - see front matter
doi:10.1016/j.engfracmech.2003.11.005

For the past decade, FGMs have been extensively investigated for various applications including synthesis of thermal barrier coatings for space-type applications [6]; first-wall composite materials in nuclear fusion and fast breeder reactors [7]; piezoelectric and thermoelectric devices, and high-density magnetic recording media and position-measuring devices [8–11]; graded refractive index materials [12]; thermionic converters [13]; dental and other implants [14,15]; and fire retardant doors [16]. New applications are continuously being discovered [5].

To pace with applications and performance demand of FGMs, scientific knowledge of fracture and damage tolerance is important for improving their structural integrity. In this paper, fracture behavior of FGMs is investigated with emphasis on the T-stress. Eischen [17] extended the eigenfunction expansion technique [18], and derived the general form of the crack-tip fields in a non-homogeneous material by assuming that the material properties are continuous, differentiable and bounded. Fig. 1 shows a crack in a two-dimensional non-homogeneous elastic body. The asymptotic stress field around the crack-tip in FGMs is given by [17]

$$\sigma_{ij}(r,\theta) = \frac{K_{\mathrm{I}}}{\sqrt{2\pi r}} f_{ij}^{\mathrm{I}}(\theta) + \frac{K_{\mathrm{II}}}{\sqrt{2\pi r}} f_{ij}^{\mathrm{II}}(\theta) + T\delta_{1i}\delta_{1j}, \quad \text{as } r \to 0, \tag{1}$$

where σ_{ij} denotes the stress tensor, K_{I} and K_{II} are the modes I and II stress intensity factors (SIFs), respectively, T is the non-singular stress, and the angular functions $f_{ij}(\theta)$ can be found in several references, e.g. [19,20]. The above stress field has the same form as the Irwin–Williams [21,18] solution for homogeneous materials. The correspondence of the crack-tip behavior between homogeneous and FGMs provides a basis for *local homogenization* near the crack-tip [22]. Thus based on the assumption that the graded material is locally homogeneous near the crack-tip, this paper establishes the relationship between the asymptotically defined interaction integral (M-integral) and T-stress, converts the M-integral to an equivalent domain integral (EDI) using auxiliary fields, and calculates the T-stress using a finite domain.

For homogeneous materials, the fracture parameters (K_{I} and K_{II}, or T) depend on the geometry, size and external loading. However, for FGMs, the fracture parameters are also affected by material gradients [17,23]. The material gradient does not affect the order of singularity and the asymptotic angular functions, but does affect the fracture parameters [17,23]. The effect of material gradient on such parameters is investigated in detail in Section 7.

For a crack under mode I conditions, the asymptotic stress field for FGMs is obtained from Eq. (1) with $K_{\mathrm{II}} = 0$. The T-stress can be best characterized by a non-dimensional parameter. Thus by normalizing the T-stress by $K_{\mathrm{I}}(\pi a)^{-1/2}$, one obtains the (stress) biaxiality ratio β given by [24]

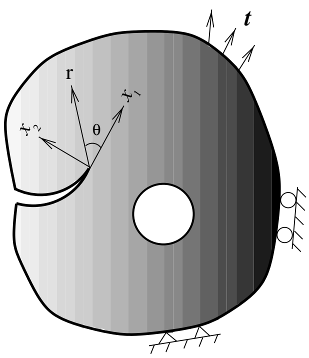

Fig. 1. Cartesian (x_1, x_2) and polar (r, θ) coordinates originating from the crack-tip in an arbitrary FGM under traction (**t**) and displacement boundary conditions.

$$\beta = \frac{T\sqrt{\pi a}}{K_{\mathrm{I}}}, \tag{2}$$

where a is the crack length. As expected, the biaxiality ratio β does depend on the geometry and loading type, but not the load magnitude, and, for FGMs, it also depends on material gradients [23]. Thus we investigate the effect of material gradients on the biaxiality ratio (β) for various graded fracture specimens.

Under small scale yielding conditions which involve high degree of triaxiality at the crack-tip, a single parameter (K_{I} or J) characterizes crack-tip conditions, and it can be used as a material property. The single parameter fracture mechanics requires that the plastic zone size (a fraction of $(K_{\mathrm{Ic}}/\sigma_{\mathrm{Y}})^2$, where σ_{Y} is the yield stress [20]) be small compared with other dimensions of the cracked structure, e.g. crack length, size of uncracked ligament, and thickness. However, under excessive plasticity, the single parameter is not sufficient to represent crack-tip fields, and fracture toughness depends on the size and geometry of the specimen. Such behavior is associated with the elastic T-stress, which affects the size and shape of the plastic zone, crack-tip constraint and fracture toughness [25–27]. In this regard, the biaxiality ratio (β) can be used as a qualitative index of the relative crack-tip constraint of various geometries [20].

The contribution of this paper includes a novel formulation of the interaction integral method to evaluate T-stress in isotropic FGMs, and benchmark solutions for the biaxiality ratio considering graded laboratory fracture specimens. The remainder of this paper is organized as follows. Section 1.1 presents a motivation to this work. Next, a brief literature review and comments on higher-order fracture parameters are presented. Section 2 provides the auxiliary fields chosen for evaluating the T-stress by means of the interaction integral (M-integral) method. Section 3 presents the interaction integral method for FGMs. Section 4 addresses the extraction of the T-stress from the M-integral. Section 5 presents some numerical aspects of the M-integral. Section 6 addresses convergence and/or accuracy of the proposed T-stress method by means of a boundary layer model. Section 7 presents several numerical examples, including verification of the T-stress solutions. Some benchmark solutions are provided for graded laboratory fracture specimens, which are useful to complement fracture testing. Finally, Section 8 concludes the work. Two appendices supplement the paper.

1.1. Motivation

This work is motivated by experimental evidence that the T-stress affects crack initiation angles [28,29]. Moreover, these angles are also affected by material non-homogeneity [30]. Material gradation can also change the sign and magnitude of the T-stress. These relevant aspects are briefly discussed below, and are elaborated upon in the remainder of the manuscript.

T-stress has a significant influence on crack initiation angles in brittle fracture [31,30]. For instance, Williams and Ewing [28] and Ueda et al. [29] performed fracture experiments on polymethylmethacrylate (PMMA), and used the "generalized maximum hoop stress criterion", which incorporates T-stress and a fracture process zone size r_c:

$$K_{\mathrm{I}}\sin\theta_0 + K_{\mathrm{II}}(3\cos\theta_0 - 1) - \frac{16}{3}T\sqrt{2\pi r_c}\sin\frac{\theta_0}{2}\cos\theta_0 = 0, \tag{3}$$

where θ_0 is the crack initiation angle. Based on such criterion, they found that negative T-stress decreases the crack initiation angle, but positive T-stress increases the angle. Fig. 2 shows experimental evidence on the T-stress effect on crack initiation angles. The experimental results obtained by Williams and Ewing [28] and Ueda et al. [29] are compared with those from the "generalized maximum hoop stress criterion" using the present finite element method (FEM), in which the SIFs and the T-stress are obtained by the interaction integral method. Notice that the above argument on the influence of the T-stress on the crack initiation angle is not restricted to a specific fracture criterion, and it is a general argument.

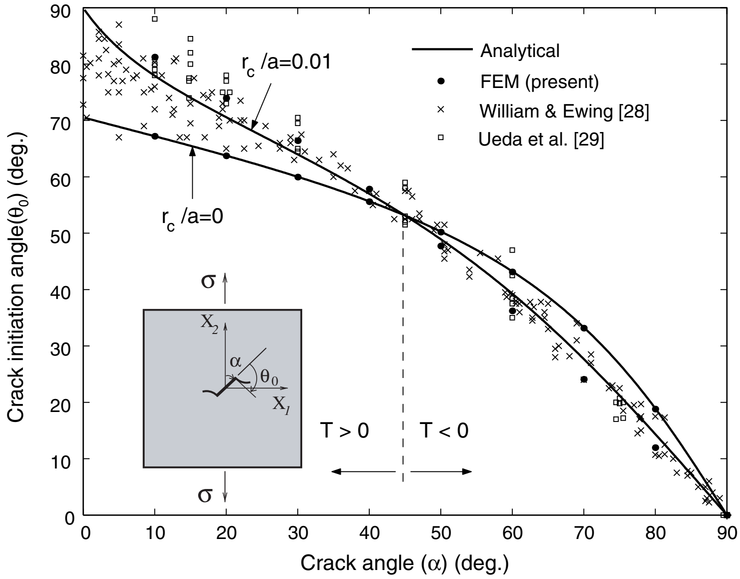

Fig. 2. Effect of the T-stress on crack initiation angles for a homogeneous PMMA plate. Experimental results are obtained from Williams and Ewing [28] and Ueda et al. [29]. The present FEM results are obtained considering an inclined center crack ($2a = 2$) in a homogeneous plate under constant traction.

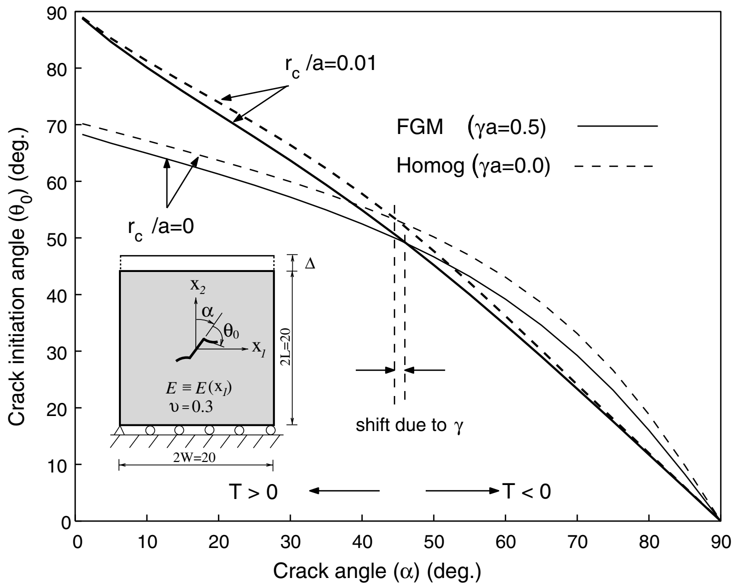

Fig. 3. Effect of material gradation on crack initiation angles predicted by the generalized maximum hoop stress criterion for the right tip of the inclined center crack ($2a = 2$) in an FGM plate under fixed-grip loading.

On the other hand, material non-homogeneity has a significant influence on crack initiation angles [30]. Fig. 3 shows comparison of crack initiation angles for the right crack-tip between homogeneous and

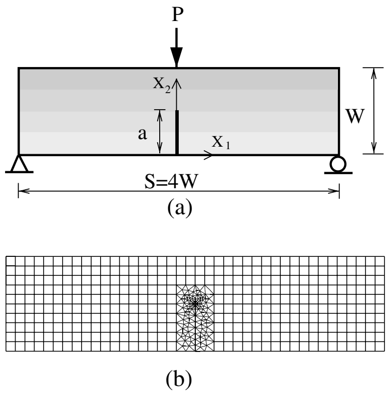

Fig. 4. Single edge notched bend (SENB) specimen: (a) geometry and boundary conditions (BCs); (b) the complete FEM mesh discretization for $a/W = 0.5$.

exponentially graded materials. There is not much effect of material non-homogeneity for a nearly horizontal ($\alpha \approx 90°$) or a nearly vertical ($\alpha \approx 0°$) crack, however, such effect is more pronounced in the mid-range of the plot (e.g. $10° < \alpha < 70°$). Notice that, for both homogeneous and FGM cases, negative T-stress decreases the crack initiation angle, but positive T-stress increases the crack initiation angle.

Material gradation has a significant influence on the sign and magnitude of T-stress and in turn the biaxiality ratio, as illustrated below for a single-edge notched bend (SENB) specimen. To further motivate the present work, Fig. 4(a) shows a graded SENB with a crack parallel to material gradation. The beam is subjected to a point load, i.e. P, at the point $(X_1, X_2) = (0, W)$. Here we consider a state of plane stress. Young's modulus is an exponential function, i.e.

$$E(X_2) = E_1 e^{\gamma X_2}, \tag{4}$$

and the Poisson's ratio is taken as constant. The following data are used for the FEM analyses (consistent units):

$$E_2/E_1 = E(W)/E(0) = (0.1 \text{ to } 10),$$

$$E_1 = 1.0, \quad \nu = 0.3, \quad S = 4W, \quad W = 1, \quad t = 1.0.$$

Fig. 4(b) shows the FEM mesh for the SENB beam. The mesh discretization consists of 408 eight-node quadrilateral (Q8) elements, 170 six-node triangular (T6) elements, and 12 six-node quarter-point triangular (T6qp) elements, with a total of 590 elements and 1200 nodes.

Fig. 5 shows the biaxiality ratio $\beta = (T\sqrt{\pi a})/K_{\mathrm{I}}$ versus a/W obtained by the present interaction integral method for the SENB specimen. Notice that, for the homogeneous SENB specimen ($E_2/E_1 = 1$), the transition point is around $a/W = 0.4$. The transition point of the sign of biaxiality ratio (and T-stress) shifts to the left as the ratio E_2/E_1 increases. For a fixed value of a/W considered here, the biaxiality ratio increases with an increasing ratio E_2/E_1. This example shows that material non-homogeneity influences the sign and magnitude of T-stress and consequently the biaxiality ratio, which in turn will affect the size and shape of the inelastic zone, crack-tip constraint and fracture toughness.

1.2. Related work

The T-stress may influence crack path stability. Considering a slight imperfection under mode I loading, Cotterell and Rice [32] found that the crack path is stable for negative T-stress, and unstable for

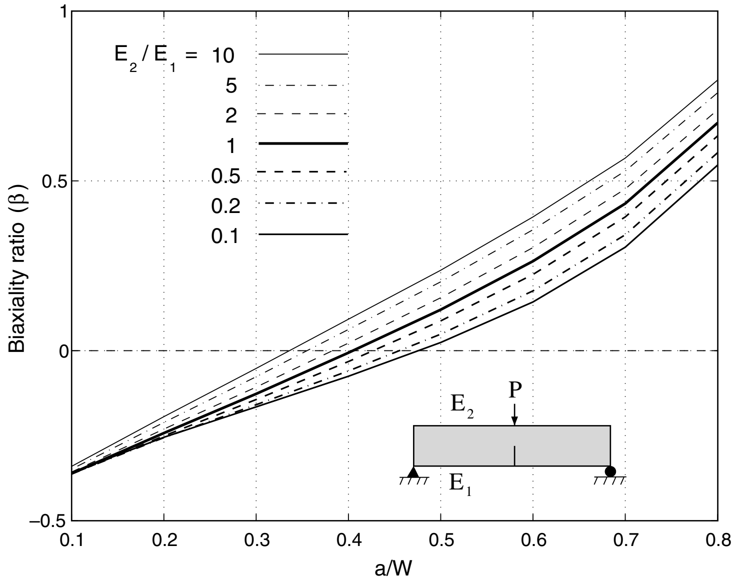

Fig. 5. Biaxiality ratio ($\beta = T\sqrt{\pi a}/K_{\mathrm{I}}$) for the single edge notched bend (SENB) specimen (see Fig. 4).

positive T-stress. Melin [33] revisited the influence of T-stress on the directional stability of cracks in conjunction with local versus global governing criteria. Such non-singular stress may also influence crack growth under mixed-mode loading [28,29,31]. For instance, based on the maximum hoop stress criterion incorporating T-stress and a fracture process zone size r_c, Williams and Ewing [28], Ueda et al. [29], and Smith et al. [31] found that negative T-stress decreases the crack initiation angle, but positive T-stress increases the angle. T-stress has also been shown to have a significant influence on crack-tip constraint and toughness [20,25–27].

The T-stress has been extensively investigated for homogeneous materials. Larsson and Carlsson [26] investigated the T-stress in mode I loading, and found that it affects the size and shape of the plastic zone, and specimens with negative T-stress have lower constraint than those with positive T-stress. They used a stress substitution method to evaluate T-stress. The stress substitution method is simple, but the accuracy of results depends on geometry, the level of mesh refinement and the radial distance considered for calculation. Leevers and Radon [24] used a variational formulation to evaluate the T-stress and biaxiality ratio. The variational approach is relatively simple to analyze external cracks, but it becomes complicated for interior cracks. Cardew et al. [34] and Kfouri [35] used the path-independent J-integral in conjunction with the interaction integral to calculate T-stress in mode I crack problems. Kfouri [35] provided two forms of Eshelby's theorem: one is the case where the traction resisted by the boundary is equal to the loads induced by the point force applied to the crack-tip, and the other is the case where the traction resisted by the boundary is not equal to the loads induced by the point force. Sherry et al. [36] investigated two- and three-dimensional cracked geometries, and provided T-stress and biaxiality ratio solutions for various laboratory specimens. Sladek et al. [37] used another type of path-independent integral, based on the Betti–Rayleigh reciprocal theorem, for evaluating T-stress in mixed-mode loading. Recently Chen et al. [38] investigated T-stress under mode I loading by means of both the Betti–Rayleigh reciprocal theorem and Eshelby's energy momentum tensor (i.e. path-independent J-integral) using the p-version finite element method, and addressed the accuracy of numerical computations. The energy-based approaches mentioned above give reasonably accurate results [34,35,37,38].

For brittle FGMs (such as $MoSi_2/SiC$ [39]), the T-stress has been shown to have a significant influence in crack initiation condition and crack initiation angle [30,40]. Becker et al. [40] investigated T-stress and finite crack kinking by using a hyperbolic-tangent function with steep gradient of Young's modulus. They found that T-stress in FGMs is affected by both the far-field loading and the far-field phase angle, and that the magnitude of T-stress in FGMs is, on average, greater than that for homogeneous materials with identical geometry. They performed finite element analyses, and calculated T-stress using the stress difference along $\theta = 0$, i.e. $\sigma_{xx} - \sigma_{yy}$. The interaction integral method is an energy-based approach, and is an accurate and robust scheme for evaluating T-stress in FGMs. Recently, Kim and Paulino [30] used the interaction integral method in conjunction with the finite element method (FEM) to investigate T-stress and its effect on crack initiation angle in FGMs, however, they used an *incompatibility formulation* [30]. This work introduces a novel *non-equilibrium formulation* of the interaction integral method in conjunction with the finite element method to evaluate T-stress in FGMs.

2. Auxiliary fields

The interaction integral method uses auxiliary fields, such as displacements ($\boldsymbol{u}^{\text{aux}}$), strains ($\boldsymbol{\varepsilon}^{\text{aux}}$), and stresses ($\boldsymbol{\sigma}^{\text{aux}}$). These auxiliary fields need to be suitably defined in order to evaluate T-stress in FGMs. There are various choices for the auxiliary fields, which may be evaluated either analytically [30] or numerically [35]. Here we adopt analytical fields originally developed for homogeneous materials and use a "non-equilibrium formulation" accounting for non-equilibrium due to the material mismatch between homogeneous and graded materials. The auxiliary fields chosen in this paper are explained below.

2.1. Displacement and strain fields

For evaluating T-stress, we choose the auxiliary displacement field due to a point force in the x_1 direction, applied to the tip of a semi-infinite crack in an infinite *homogeneous* body as shown in Fig. 6. The auxiliary displacements and strains are given by Michell's solution [41]

$$u_1^{\text{aux}} = -\frac{F(1+\kappa_{\text{tip}})}{8\pi\mu_{\text{tip}}} \ln\frac{r}{d} - \frac{F}{4\pi\mu_{\text{tip}}} \sin^2\theta, \tag{5}$$

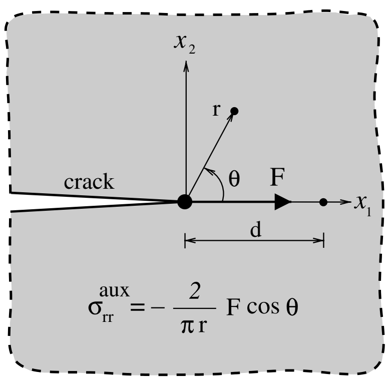

Fig. 6. A point force applied at the crack-tip in the direction parallel to the crack in an infinite homogeneous medium—Michell's solution [41].

$$u_2^{\text{aux}} = -\frac{F(\kappa_{\text{tip}} - 1)}{8\pi\mu_{\text{tip}}}\theta + \frac{F}{4\pi\mu_{\text{tip}}}\sin\theta\cos\theta \tag{6}$$

and

$$\varepsilon_{ij}^{\text{aux}} = (u_{i,j}^{\text{aux}} + u_{j,i}^{\text{aux}})/2 \quad (i,j = 1,2), \tag{7}$$

where F is the point force applied at the crack-tip, d is the coordinate of a fixed point on the x_1 axis (see Fig. 6), μ_{tip} is the shear modulus evaluated at the crack-tip, and

$$\kappa_{\text{tip}} = \begin{cases} (3 - \nu_{\text{tip}})/(1 + \nu_{\text{tip}}) & \text{plane stress}, \\ (3 - 4\nu_{\text{tip}}) & \text{plane strain} \end{cases} \tag{8}$$

in which ν_{tip} denotes the Poisson's ratio at the crack-tip location.

2.2. Stress field

The non-equilibrium formulation is based on the fact that the auxiliary stress field given by

$$\sigma_{ij}^{\text{aux}} = C_{ijkl}(\boldsymbol{x})\varepsilon_{kl}^{\text{aux}} \tag{9}$$

does not satisfy equilibrium because it differs from

$$\sigma_{ij}^{\text{aux}} = (C_{ijkl})_{\text{tip}}\varepsilon_{kl}^{\text{aux}}, \tag{10}$$

where $C_{ijkl}(\boldsymbol{x})$ is the constitutive tensor of FGMs, and $(C_{ijkl})_{\text{tip}}$ is the constitutive tensor evaluated at the crack-tip (see Fig. 7). The derivatives of the auxiliary stress field (Eq. (9)) are

$$\begin{aligned} \sigma_{ij,j}^{\text{aux}} &= C_{ijkl,j}(\boldsymbol{x})\varepsilon_{kl}^{\text{aux}} + C_{ijkl}(\boldsymbol{x})\varepsilon_{kl,j}^{\text{aux}} \\ &= \underline{(C_{ijkl})_{\text{tip}}\varepsilon_{kl,j}^{\text{aux}}} + C_{ijkl,j}(\boldsymbol{x})\varepsilon_{kl}^{\text{aux}} + (C_{ijkl}(\boldsymbol{x}) - (C_{ijkl})_{\text{tip}})\varepsilon_{kl,j}^{\text{aux}}, \end{aligned} \tag{11}$$

where the underlined term in Eq. (11) vanishes because it satisfies equilibrium for homogeneous materials. Thus Eq. (11) becomes

$$\sigma_{ij,j}^{\text{aux}} = \left[C_{ijkl,j}(\boldsymbol{x})\varepsilon_{kl}^{\text{aux}} + (C_{ijkl}(\boldsymbol{x}) - (C_{ijkl})_{\text{tip}})\varepsilon_{kl,j}^{\text{aux}}\right] \neq 0, \tag{12}$$

where the second term in Eq. (12) vanishes for the special case where the constitutive tensor $C_{ijkl}(\boldsymbol{x})$ is proportional to $(C_{ijkl})_{\text{tip}}$. This choice of the auxiliary fields has been discussed by Dolbow and Gosz [42], but

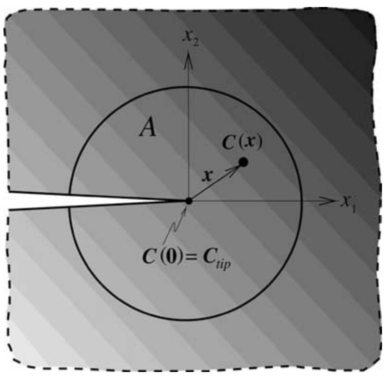

Fig. 7. Illustration of the interaction integral formulation considering material non-homogeneity. Notice that $C(\boldsymbol{x}) \neq C_{\text{tip}}$ for $\boldsymbol{x} \neq \mathbf{0}$. The area A denotes a representative region around the crack-tip.

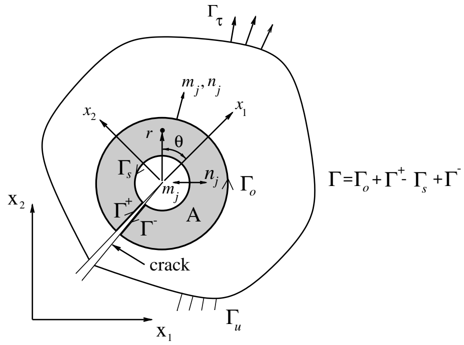

Fig. 8. Conversion of the contour integral into an equivalent domain integral (EDI). Here $\Gamma = \Gamma_o + \Gamma^+ - \Gamma_s + \Gamma^-$, $m_j = n_j$ on Γ_o and $m_j = -n_j$ on Γ_s.

the non-equilibrium formulation was not provided in their paper. The non-equilibrium in the stress field is considered in the interaction integral formulation, which is discussed below.

3. The interaction integral: M-integral

The interaction integral (M-integral [1]) is a two-state integral, which is derived from the path-independent J-integral [47] for two admissible states of a cracked elastic FGM body. The standard J-integral [47] is given by

$$J = \lim_{\Gamma_s \to 0} \int_{\Gamma_s} (\mathscr{W}\delta_{1j} - \sigma_{ij}u_{i,1})n_j \, \mathrm{d}\Gamma, \tag{13}$$

where $\mathscr{W}$ is the strain energy density expressed by

$$\mathscr{W} = \frac{1}{2}\sigma_{ij}\varepsilon_{ij} = \frac{1}{2}C_{ijkl}\varepsilon_{kl}\varepsilon_{ij}, \tag{14}$$

and n_j is the outward normal vector to the contour Γ_s, as shown in Fig. 8. To convert the contour integral into an equivalent domain integral (EDI) [48], the following contour integral is defined:

$$\mathscr{H} = \oint_{\Gamma} (W\delta_{1j} - \sigma_{ij}u_{i,1})m_j q \, \mathrm{d}\Gamma, \tag{15}$$

where $\Gamma = \Gamma_o + \Gamma^+ - \Gamma_s + \Gamma^-$, m_j is a unit vector outward normal to the corresponding contour (i.e. $m_j = n_j$ on Γ_o and $m_j = -n_j$ on Γ_s), and q is a weight function, which varies from $q = 1$ on Γ_s to $q = 0$ on Γ_o (see Fig. 9). Taking the limit $\Gamma_s \to 0$ leads to [30]

$$\lim_{\Gamma_s \to 0} \mathscr{H} = \lim_{\Gamma_s \to 0} \left[\int_{\Gamma_o + \Gamma^+ + \Gamma^-} (\mathscr{W}\delta_{1j} - \sigma_{ij}u_{i,1})m_j q \, \mathrm{d}\Gamma - \int_{\Gamma_s} (\mathscr{W}\delta_{1j} - \sigma_{ij}u_{i,1})n_j q \, \mathrm{d}\Gamma \right]. \tag{16}$$

Because $q = 0$ on Γ_o and the crack faces are assumed to be traction-free, Eq. (16) becomes

[1] Here, the so-called M-integral should not be confused with the M-integral (conservation integral) of Knowles and Sternberg [43], Budiansky and Rice [44], and Chang and Chien [45]. Also, see the book by Kanninen and Popelar [46] for a review of conservation integrals in fracture mechanics.

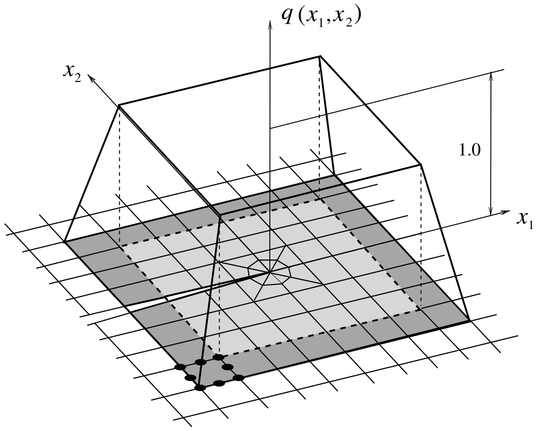

Fig. 9. Plateau weight function (q-function).

$$J = -\lim_{\Gamma_s \to 0} \mathscr{H} = -\lim_{\Gamma_s \to 0} \oint_{\Gamma} (\mathscr{W}\delta_{1j} - \sigma_{ij}u_{i,1})m_j q\,\mathrm{d}\Gamma. \tag{17}$$

Applying the divergence theorem to Eq. (17) and using the weight function q, one obtains the EDI as

$$J = \int_A (\sigma_{ij}u_{i,1} - \mathscr{W}\delta_{1j})q_{,j}\,\mathrm{d}A + \int_A (\sigma_{ij}u_{i,1} - \mathscr{W}\delta_{1j})_{,j} q\,\mathrm{d}A. \tag{18}$$

The J-integral of the superimposed fields (actual and auxiliary fields) is given as:

$$\begin{aligned} J^{\mathrm{s}} = & \int_A \left\{ (\sigma_{ij} + \sigma_{ij}^{\mathrm{aux}})(u_{i,1} + u_{i,1}^{\mathrm{aux}}) - \frac{1}{2}(\sigma_{ik} + \sigma_{ik}^{\mathrm{aux}})(\varepsilon_{ik} + \varepsilon_{ik}^{\mathrm{aux}})\delta_{1j} \right\} q_{,j}\,\mathrm{d}A \\ & + \int_A \left\{ (\sigma_{ij} + \sigma_{ij}^{\mathrm{aux}})(u_{i,1} + u_{i,1}^{\mathrm{aux}}) - \frac{1}{2}(\sigma_{ik} + \sigma_{ik}^{\mathrm{aux}})(\varepsilon_{ik} + \varepsilon_{ik}^{\mathrm{aux}})\delta_{1j} \right\}_{,j} q\,\mathrm{d}A, \end{aligned} \tag{19}$$

which is conveniently decomposed into

$$J^{\mathrm{s}} = J + J^{\mathrm{aux}} + M, \tag{20}$$

where J^{aux} is given by

$$J^{\mathrm{aux}} = \int_A (\sigma_{ij}^{\mathrm{aux}} u_{i,1}^{\mathrm{aux}} - \mathscr{W}^{\mathrm{aux}}\delta_{1j})q_{,j}\,\mathrm{d}A + \int_A \left\{ \sigma_{ij}^{\mathrm{aux}} u_{i,1}^{\mathrm{aux}} - \frac{1}{2}\sigma_{ik}^{\mathrm{aux}}\varepsilon_{ik}^{\mathrm{aux}}\delta_{1j} \right\}_{,j} q\,\mathrm{d}A, \tag{21}$$

and the resulting general form of the interaction integral (M) is given by

$$\begin{aligned} M = & \int_A \left\{ \sigma_{ij}u_{i,1}^{\mathrm{aux}} + \sigma_{ij}^{\mathrm{aux}}u_{i,1} - \frac{1}{2}(\sigma_{ik}\varepsilon_{ik}^{\mathrm{aux}} + \sigma_{ik}^{\mathrm{aux}}\varepsilon_{ik})\delta_{1j} \right\} q_{,j}\,\mathrm{d}A \\ & + \int_A \left\{ \sigma_{ij}u_{i,1}^{\mathrm{aux}} + \sigma_{ij}^{\mathrm{aux}}u_{i,1} - \frac{1}{2}(\sigma_{ik}\varepsilon_{ik}^{\mathrm{aux}} + \sigma_{ik}^{\mathrm{aux}}\varepsilon_{ik})\delta_{1j} \right\}_{,j} q\,\mathrm{d}A. \end{aligned} \tag{22}$$

3.1. Non-equilibrium formulation

The specific interaction integral (M), based on the non-equilibrium formulation, is derived here. Using the following identity:

$$\sigma_{ij}\varepsilon_{ij}^{\mathrm{aux}} = C_{ijkl}(\boldsymbol{x})\varepsilon_{kl}\varepsilon_{ij}^{\mathrm{aux}} = \sigma_{kl}^{\mathrm{aux}}\varepsilon_{kl} = \sigma_{ij}^{\mathrm{aux}}\varepsilon_{ij}, \tag{23}$$

one rewrites Eq. (22) as

$$M = \int_A \left\{\sigma_{ij}u_{i,1}^{\mathrm{aux}} + \sigma_{ij}^{\mathrm{aux}}u_{i,1} - \sigma_{ik}\varepsilon_{ik}^{\mathrm{aux}}\delta_{1j}\right\}q_{,j}\,\mathrm{d}A + \int_A \left\{\sigma_{ij}u_{i,1}^{\mathrm{aux}} + \sigma_{ij}^{\mathrm{aux}}u_{i,1} - \sigma_{ik}\varepsilon_{ik}^{\mathrm{aux}}\delta_{1j}\right\}_{,j}q\,\mathrm{d}A = M_1 + M_2. \tag{24}$$

Moreover, the last term of the second integral (M_2) in Eq. (24) is expressed as

$$\begin{aligned}(\sigma_{ik}\varepsilon_{ik}^{\mathrm{aux}}\delta_{1j})_{,j} &= (\sigma_{ik}\varepsilon_{ik}^{\mathrm{aux}})_{,1} = (\sigma_{ij}\varepsilon_{ij}^{\mathrm{aux}})_{,1} = (C_{ijkl}\varepsilon_{kl}\varepsilon_{ij}^{\mathrm{aux}})_{,1} \\ &= C_{ijkl,1}\varepsilon_{kl}\varepsilon_{ij}^{\mathrm{aux}} + C_{ijkl}\varepsilon_{kl,1}\varepsilon_{ij}^{\mathrm{aux}} + C_{ijkl}\varepsilon_{kl}\varepsilon_{ij,1}^{\mathrm{aux}} \\ &= C_{ijkl,1}\varepsilon_{kl}\varepsilon_{ij}^{\mathrm{aux}} + \sigma_{ij}^{\mathrm{aux}}\varepsilon_{ij,1} + \sigma_{ij}\varepsilon_{ij,1}^{\mathrm{aux}}.\end{aligned} \tag{25}$$

Substitution of Eq. (25) into Eq. (24) leads to

$$M_2 = \int_A \left(\sigma_{ij,j}u_{i,1}^{\mathrm{aux}} + \sigma_{ij}u_{i,1j}^{\mathrm{aux}} + \sigma_{ij,j}^{\mathrm{aux}}u_{i,1} + \sigma_{ij}^{\mathrm{aux}}u_{i,1j}\right)q\,\mathrm{d}A - \int_A \left(C_{ijkl,1}\varepsilon_{kl}\varepsilon_{ij}^{\mathrm{aux}} + \sigma_{ij}^{\mathrm{aux}}\varepsilon_{ij,1} + \sigma_{ij}\varepsilon_{ij,1}^{\mathrm{aux}}\right)q\,\mathrm{d}A. \tag{26}$$

Using compatibility (actual and auxiliary) and equilibrium (actual) (i.e. $\sigma_{ij,j} = 0$ with no body force), one simplifies Eq. (26) as

$$M_2 = \int_A \left\{\sigma_{ij,j}^{\mathrm{aux}}u_{i,1} - C_{ijkl,1}\varepsilon_{kl}\varepsilon_{ij}^{\mathrm{aux}}\right\}q\,\mathrm{d}A. \tag{27}$$

Therefore the resulting interaction integral (M) becomes

$$M = \int_A \left\{\sigma_{ij}u_{i,1}^{\mathrm{aux}} + \sigma_{ij}^{\mathrm{aux}}u_{i,1} - \sigma_{ik}\varepsilon_{ik}^{\mathrm{aux}}\delta_{1j}\right\}q_{,j}\,\mathrm{d}A + \int_A \left\{\underline{\sigma_{ij,j}^{\mathrm{aux}}u_{i,1}} - C_{ijkl,1}\varepsilon_{kl}\varepsilon_{ij}^{\mathrm{aux}}\right\}q\,\mathrm{d}A, \tag{28}$$

where the underlined term is a non-equilibrium term that appears due to non-equilibrium of the auxiliary stress fields (see Section 2.2), which must be considered to obtain converged solutions. Other alternative formulations are the incompatibility and the constant-constitutive-tensor formulations, which are discussed in Appendix A.

3.2. Proof of the existence of the M-integral for FGMs

The second integral in Eq. (28) involves the extra terms arising due to material non-homogeneity. The existence of the integral as the limit $r \to 0$ is proved below. The constitutive tensor involving material properties $E(r,\theta)$ and $\nu(r,\theta)$ must be continuous and differentiable function, and thus it can be written as [17]

$$C_{ijkl}(r,\theta) = (C_{ijkl})_{\mathrm{tip}} + rC_{ijkl}^{(1)}(\theta) + \frac{r^2}{2}C_{ijkl}^{(2)}(\theta) + \mathrm{O}(r^3) + \cdots, \tag{29}$$

where $C_{ijkl}^{(n)}(\theta)$ $(n = 1,2,\ldots)$ are angular functions. In Eq. (11), the first term vanishes because of equilibrium, the second term vanishes because of smoothness assumption of the constitutive tensor, and here we focus on the third term only. For the auxiliary fields for T-stress ($\boldsymbol{u}^{\mathrm{aux}} = \mathrm{O}(\ln r)$, $\boldsymbol{\varepsilon}^{\mathrm{aux}} = \mathrm{O}(r^{-1})$), the integral involving the non-equilibrium term, as the limit r goes to zero, becomes

$$\begin{aligned}\lim_{A\to 0}\int_A \sigma_{ij,j}^{\mathrm{aux}} u_{i,1} q\,\mathrm{d}A &= \lim_{r\to 0}\int_\theta\int_r \sigma_{ij,j}^{\mathrm{aux}} u_{i,1} qr\,\mathrm{d}r\,\mathrm{d}\theta \\ &= \lim_{r\to 0}\int_\theta\int_r (C_{ijkl}(r,\theta)-(C_{ijkl})_{\mathrm{tip}})\varepsilon_{kl,j}^{\mathrm{aux}} u_{i,1} qr\,\mathrm{d}r\,\mathrm{d}\theta \\ &= \lim_{r\to 0}\int_\theta\int_r \mathrm{O}(r)\mathrm{O}(r^{-2})\mathrm{O}(r^{-1/2}) qr\,\mathrm{d}r\,\mathrm{d}\theta \\ &= \lim_{r\to 0}\mathrm{O}(r^{1/2}) = 0. \end{aligned} \tag{30}$$

The integral involving material derivatives ($C_{ijkl,1}$) in Eq. (28) vanishes for the following reason. Derivatives of the elastic moduli are assumed to be bounded at the crack-tip, i.e. $C_{ijkl,1}$ is $\mathrm{O}(r^\alpha)$ with $\alpha \geqslant 0$. Therefore, as the limit r goes to zero, the integral becomes

$$\begin{aligned}\lim_{A\to 0}\int_A C_{ijkl,1}\varepsilon_{kl}\varepsilon_{ij}^{\mathrm{aux}} q\,\mathrm{d}A &= \lim_{r\to 0}\int_\theta\int_r C_{ijkl,1}\varepsilon_{kl}\varepsilon_{ij}^{\mathrm{aux}} qr\,\mathrm{d}r\,\mathrm{d}\theta \\ &= \lim_{r\to 0}\int_\theta\int_r \mathrm{O}(r^\alpha)\mathrm{O}(r^{-1/2})\mathrm{O}(r^{-1}) qr\,\mathrm{d}r\,\mathrm{d}\theta \\ &= \lim_{r\to 0}\mathrm{O}(r^{\alpha+1/2}) = 0. \end{aligned} \tag{31}$$

Thus the limit exists and the proposed integral is well posed.

3.3. Exponentially graded materials

Materials with exponential gradation have been extensively investigated in the technical literature, e.g. [23,42,49–65], and thus a specific form of the M-integral is derived for such type of material gradation. For the sake of simplicity, we consider an exponentially graded material in which Poisson's ratio is constant and Young's modulus varies in X_1 direction (see Fig. 10), i.e.

$$E(X_1) = E_0\exp(\gamma X_1), \qquad v = \text{constant}, \tag{32}$$

where γ is the material non-homogeneity parameter and $1/\gamma$ denotes the length scale of non-homogeneity.

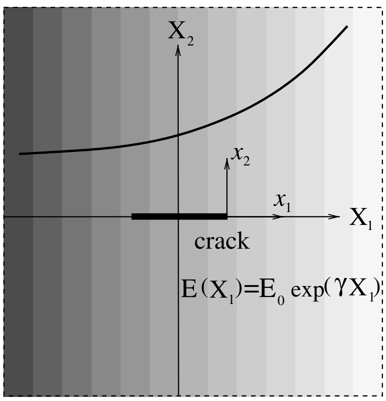

Fig. 10. Crack parallel to material gradation in an exponentially graded material. The notation (X_1, X_2) denotes global coordinate system, and the notation (x_1, x_2) denotes crack-tip local coordinates.

The derivatives of interest are (see Eq. (28))

$$\begin{aligned}\sigma_{ij,j}^{\mathrm{aux}} &= C_{ijkl,j}(x_1)\varepsilon_{kl}^{\mathrm{aux}} + C_{ijkl}(x_1)\varepsilon_{kl,j}^{\mathrm{aux}} \\ &= \gamma\sigma_{ij}^{\mathrm{aux}}\delta_{1j} + \alpha_{\mathrm{p}}(C_{ijkl})_{\mathrm{tip}}\varepsilon_{kl,j}^{\mathrm{aux}} \\ &= \gamma\sigma_{ij}^{\mathrm{aux}}\delta_{1j},\end{aligned} \tag{33}$$

$$C_{ijkl,1} = \gamma C_{ijkl}(x_1), \tag{34}$$

where $\alpha_{\mathrm{p}} = \exp(\gamma x_1)$ is a proportionality factor. Substitution of Eqs. (33) and (34) into Eq. (28) yields the specific form of the interaction integral

$$M = \int_A \left\{ \sigma_{ij}u_{i,1}^{\mathrm{aux}} + \sigma_{ij}^{\mathrm{aux}}u_{i,1} - \sigma_{ik}\varepsilon_{ik}^{\mathrm{aux}}\delta_{1j} \right\} q_{,j}\,\mathrm{d}A + \int_A \left\{ \gamma\sigma_{ij}^{\mathrm{aux}}u_{i,1}\delta_{1j} - \gamma\sigma_{ij}\varepsilon_{ij}^{\mathrm{aux}} \right\} q\,\mathrm{d}A. \tag{35}$$

The derivatives of material properties are represented by the material non-homogeneity parameter γ, and the contribution of the non-equilibrium term to the M-integral is also related to the value of γ. Notice that, for this particular case of material variation (see Eq. (32)), a simpler expression than that for the general case (Eq. (28)) is obtained.

4. Extraction of *T*-stress

The T-stress can be extracted from the interaction integral taking the limit $r \to 0$ of the domain A shown in Fig. 8. By doing so, the contributions of the higher-order (i.e. $\mathrm{O}(r^{1/2})$ and higher) and singular (i.e. $\mathrm{O}(r^{-1/2})$) terms vanish.

Eq. (22) is rewritten as

$$M_{\mathrm{local}} = \int_A \left[\left\{ (\sigma_{ij}u_{i,1}^{\mathrm{aux}} + \sigma_{ij}^{\mathrm{aux}}u_{i,1}) - \frac{1}{2}(\sigma_{ik}\varepsilon_{ik}^{\mathrm{aux}} + \sigma_{ik}^{\mathrm{aux}}\varepsilon_{ik})\delta_{1j} \right\} q \right]_{,j} \mathrm{d}A, \tag{36}$$

where M_{local} denotes the M-integral with respect to local coordinates (x_1, x_2) (see Fig. 8). By applying the divergence theorem to Eq. (36), one obtains

$$M_{\mathrm{local}} = \lim_{\Gamma_{\mathrm{s}} \to 0} \oint_{\Gamma} \left\{ (\sigma_{ij}u_{i,1}^{\mathrm{aux}} + \sigma_{ij}^{\mathrm{aux}}u_{i,1}) - \frac{1}{2}(\sigma_{ik}\varepsilon_{ik}^{\mathrm{aux}} + \sigma_{ik}^{\mathrm{aux}}\varepsilon_{ik})\delta_{1j} \right\} m_j q\,\mathrm{d}\Gamma. \tag{37}$$

Because $m_j = -n_j$ and $q = 1$ on Γ_{s}, $m_j = n_j$ and $q = 0$ on Γ_{o}, and the crack faces are assumed to be traction-free, Eq. (37) becomes

$$M_{\mathrm{local}} = \lim_{\Gamma_{\mathrm{s}} \to 0} \int_{\Gamma_{\mathrm{s}}} \left[\frac{1}{2}(\sigma_{ik}\varepsilon_{ik}^{\mathrm{aux}} + \sigma_{ik}^{\mathrm{aux}}\varepsilon_{ik})\delta_{1j} - (\sigma_{ij}u_{i,1}^{\mathrm{aux}} + \sigma_{ij}^{\mathrm{aux}}u_{i,1}) \right] n_j\,\mathrm{d}\Gamma. \tag{38}$$

Using the equality in Eq. (23), one reduces Eq. (38) to

$$M_{\mathrm{local}} = \lim_{\Gamma_{\mathrm{s}} \to 0} \int_{\Gamma_{\mathrm{s}}} \left[\sigma_{ik}\varepsilon_{ik}^{\mathrm{aux}}\delta_{1j} - (\sigma_{ij}u_{i,1}^{\mathrm{aux}} + \sigma_{ij}^{\mathrm{aux}}u_{i,1}) \right] n_j\,\mathrm{d}\Gamma. \tag{39}$$

The actual stress fields are given by

$$\sigma_{ij} = K_{\mathrm{I}}(2\pi r)^{-1/2} f_{ij}^{\mathrm{I}}(\theta) + K_{\mathrm{II}}(2\pi r)^{-1/2} f_{ij}^{\mathrm{II}}(\theta) + T\delta_{1i}\delta_{1j} + \mathrm{O}(r^{1/2}), \tag{40}$$

where the angular functions $f_{ij}^{\mathrm{I}}(\theta)$ and $f_{ij}^{\mathrm{II}}(\theta)$ $(i, j = 1, 2)$ are given, for example, in Ref. [19]. As the contour Γ_{s} (see Fig. 8) shrinks to the crack-tip region, the higher-order terms cancel out as mentioned above. Moreover, there is no contribution from the singular terms $\mathrm{O}(r^{-1/2})$ because the integrations from $\theta = -\pi$

to $+\pi$ of angular functions (coefficients) of the three terms given in Eq. (39) are cancelled out, and become zero regardless of the resulting singularity $\mathrm{O}(r^{-1/2})$.

According to the above argument, the only term that contributes to M is the term involving T. Therefore, Eq. (40) simplifies to the following expression:

$$\sigma_{ij} = T\delta_{1i}\delta_{1j}, \tag{41}$$

which refers to the stress parallel to the crack direction. Substituting Eq. (41) into Eq. (39), one obtains

$$M_{\mathrm{local}} = -\lim_{\Gamma_s \to 0} \int_{\Gamma_s} \sigma_{ij}^{\mathrm{aux}} n_j u_{i,1}\, \mathrm{d}\Gamma = -\frac{T}{E_{\mathrm{tip}}^*} \lim_{\Gamma_s \to 0} \int_{\Gamma_s} \sigma_{ij}^{\mathrm{aux}} n_j\, \mathrm{d}\Gamma. \tag{42}$$

Because the force F is in equilibrium (Fig. 6)

$$F = -\lim_{\Gamma_s \to 0} \int_{\Gamma_s} \sigma_{ij}^{\mathrm{aux}} n_j\, \mathrm{d}\Gamma, \tag{43}$$

and thus the T-stress is derived as

$$T = \frac{E_{\mathrm{tip}}^*}{F} M_{\mathrm{local}}, \tag{44}$$

where

$$E_{\mathrm{tip}}^* = \begin{cases} E_{\mathrm{tip}} & \text{plane stress,} \\ E_{\mathrm{tip}}/(1-\nu_{\mathrm{tip}}^2) & \text{plane strain.} \end{cases} \tag{45}$$

Similar arguments have been used by Kim and Paulino [30] to extract the T-stress in FGMs using an incompatibility formulation.

5. Some numerical aspects

For numerical computation by means of the FEM, the M-integral is evaluated first in global coordinates (M_{global}) and then transformed to local coordinates (M_{local}). Thus the global interaction integral $(M_m)_{\mathrm{global}}$ $(m = 1, 2)$ is obtained as $(m = 1, 2)$:

$$(M_m)_{\mathrm{global}} = \int_A \left\{ \sigma_{ij} u_{i,m}^{\mathrm{aux}} + \sigma_{ij}^{\mathrm{aux}} u_{i,m} - \sigma_{ik}\varepsilon_{ik}^{\mathrm{aux}} \delta_{mj} \right\} \frac{\partial q}{\partial X_j}\, \mathrm{d}A + \int_A \left\{ \sigma_{ij,j}^{\mathrm{aux}} u_{i,m} - C_{ijkl,m}\varepsilon_{kl}\varepsilon_{ij}^{\mathrm{aux}} \right\} q\, \mathrm{d}A, \tag{46}$$

where (X_1, X_2) are the global coordinates shown in Fig. 8. Therefore one obtains M_{local} as

$$M_{\mathrm{local}} = (M_1)_{\mathrm{local}} = (M_1)_{\mathrm{global}} \cos\theta + (M_2)_{\mathrm{global}} \sin\theta. \tag{47}$$

For the sake of generality, we determine derivatives of material properties using shape function derivatives of finite elements [23,62]. The derivatives of the auxiliary stress field are obtained as

$$\sigma_{ij,j}^{\mathrm{aux}} = C_{ijkl,j}\varepsilon_{kl}^{\mathrm{aux}} + C_{ijkl}\varepsilon_{kl,j}^{\mathrm{aux}}, \tag{48}$$

which requires the derivatives of the constitutive tensor $\mathbf{C}$. A simple and accurate numerical approach consists of evaluating the derivatives of the $\mathbf{C}$ tensor (see Eqs. (46) and (48)) by means of shape function derivatives. Thus the spatial derivatives of a generic material quantity P (e.g. C_{ijkl}) are obtained as

$$\frac{\partial P}{\partial X_m} = \sum_{i=1}^{n} \frac{\partial N_i}{\partial X_m} P_i \quad (m = 1, 2), \tag{49}$$

where n is the number of nodes in the graded element, and $N_i = N_i(\xi, \eta)$ are the element shape functions which can be found in many FEM references, e.g. [66]. The derivatives $\partial N_i/\partial X_m$ are obtained as

$$\left\{ \begin{array}{l} \partial N_i/\partial X_1 \\ \partial N_i/\partial X_2 \end{array} \right\} = \boldsymbol{J}^{-1} \left\{ \begin{array}{l} \partial N_i/\partial \xi \\ \partial N_i/\partial \eta \end{array} \right\}, \tag{50}$$

where $\boldsymbol{J}^{-1}$ is the inverse of the standard Jacobian matrix relating (X_1, X_2) with (ξ, η) [66].

6. Boundary layer model

Here we investigate convergence and accuracy of T-stress by using a boundary layer model for homogeneous and functionally graded materials. Fig. 11(a) illustrates a boundary layer model, and Fig. 11(b) shows the FEM mesh discretization which consists of 1802 Q8, 50 T6, and 18 T6qp elements, with a total of 1870 elements and 5689 nodes.

The circular boundary contour is subjected to the following near-tip displacements [17,18]:

$$\begin{aligned} u_1 &= \frac{K_\mathrm{I}}{4\mu_{\mathrm{tip}}} \sqrt{\frac{r}{2\pi}} \left\{ (2\kappa_{\mathrm{tip}} - 1) \cos\frac{\theta}{2} - \cos\frac{3\theta}{2} \right\} + \frac{Tr}{E_{\mathrm{tip}}} \cos\theta, \\ u_2 &= \frac{K_\mathrm{I}}{4\mu_{\mathrm{tip}}} \sqrt{\frac{r}{2\pi}} \left\{ (2\kappa_{\mathrm{tip}} + 1) \sin\frac{\theta}{2} - \sin\frac{3\theta}{2} \right\} - \frac{Tr\nu_{\mathrm{tip}}}{E_{\mathrm{tip}}} \sin\theta. \end{aligned} \tag{51}$$

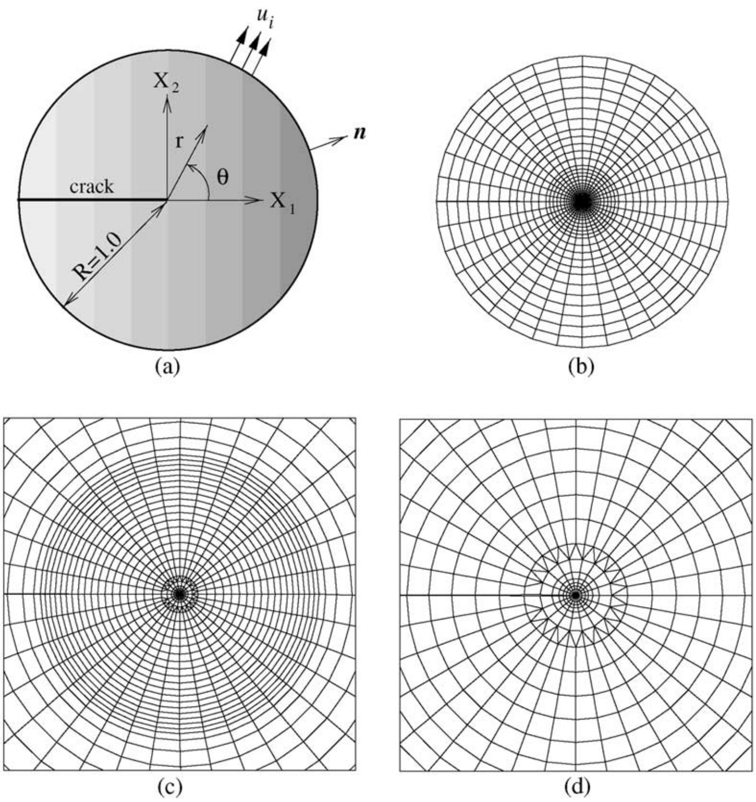

Fig. 11. A boundary layer model: (a) boundary layer model subjected to displacement (u_i) loading (see Eq. (51)); (b) the complete finite element mesh; (c) zoom of a crack-tip region; (d) zoom of (c) very near the crack-tip.

Table 1
Convergence and/or accuracy of T-stress using a boundary layer model. Displacements u_i $(i = 1, 2)$ are applied along the circular boundary considering $K_{\mathrm{I}} = 1.0$ and $T = 1.0$ (consistent units)

Domain	Radius of domain	T-stress	
		$\gamma a = 0.0$	$\gamma a = 0.5$
1	0.00101	0.9716	1.29590
2	0.00136	0.9760	1.24775
3	0.00186	0.9766	1.21322
4	0.00284	0.9800	1.18323
5	0.00411	0.9861	1.16557
6	0.00608	0.9937	1.15826
7	0.00800	0.9947	1.15657
8	0.01510	0.9958	1.15589
9	0.01836	0.9960	1.15589
10	0.03125	0.9965	1.15608
11	0.10833	0.9979	1.15701
12	0.20	0.9992	1.15847
13	0.40	1.0003	1.15965

The Young's modulus varies exponentially and the Poisson's ratio is constant (see Fig. 11(a)):

$$E(X_1) = E_0 \exp(\gamma X_1), \qquad \nu = \text{constant}, \tag{52}$$

where γ is the material non-homogeneity parameter and $1/\gamma$ denotes the length scale of non-homogeneity. The following data are used for the FEM analyses:

$$\begin{aligned} &\text{plane stress},\ 2 \times 2 \text{ Gauss quadrature}, \\ &a = 1, \quad R = 1, \\ &\gamma a = (0, 0.5), \\ &E_0 = 1.0, \quad \nu = 0.3. \end{aligned} \tag{53}$$

Table 1 shows FEM results for the T-stress considering displacements u_i $(i = 1, 2)$ in Eq. (51) applied along the boundary with $K_{\mathrm{I}} = 1.0$ and $T = 1.0$ (consistent units) for homogeneous ($\gamma a = 0.0$) and graded ($\gamma a = 0.5$) materials. For homogeneous materials, as the domain becomes large, the T-stress converges to the exact solution ($T = 1.0$), and thus its accuracy increases. For the FGM case, the exact solution is not available, but the T-stress tends to converge. Notice that the T-stress shows larger domain dependence for non-homogeneous than for homogeneous materials.

7. Numerical examples and discussions

To assess the non-equilibrium formulation of the interaction integral method for evaluating T-stress by means of the FEM, the following numerical examples are presented:

- Inclined center crack in a plate:
  (1) constant traction—homogeneous material case,
  (2) fixed-grip loading—FGM case;
- Benchmark examples based on laboratory specimens:
  (1) single edge notched tension (SENT),
  (2) double edge notched tension (DENT),
  (3) center cracked tension (CCT),

   (4) single edge notched bending (SENB),
   (5) compact tension (CT);
- On scaling of FGM specimens;
- Internal crack in a strip;
- Slanted edge crack in a plate;
- Internal or edge crack in a circular disk;
- Three-point bending specimen with a crack perpendicular to material gradation.

The FEM code I-FRANC2D (Illinois-FRANC2D) is used for implementation of the interaction integral formulation, and for evaluating T-stress in all the numerical results presented in this paper. The code I-FRANC2D is based on the code FRANC2D (FRacture ANalysis Code 2D) [67,68], which was originally developed at Cornell University. The extended capabilities of I-FRANC2D include graded elements to discretize non-homogeneous materials, and fracture parameters such as T-stress and SIFs. The graded elements are based on the "generalized isoparametric formulation" or GIF [23] and, in general, they show superior performance to conventional homogeneous elements [62]. An alternative approach consists of using direct Gaussian integration formulation, in which the material properties are evaluated directly at the Gauss points (see [23,63]). Using graded elements and the GIF, the I-FRANC2D code can evaluate T-stress for FGMs by means of the interaction integral.

Isoparametric graded elements are used to discretize all the geometry. Singular quarter-point six-node triangles (T6qp) are used for crack-tip elements, eight-node serendipity elements (Q8) are used for a circular region around crack-tip elements and over most of the mesh, and regular six-node triangles (T6) are used in the transition zone between regions of Q8 elements. For T6 and T6qp elements, four-point Gauss quadrature is used. For Q8 elements, 2×2 reduced Gauss quadrature is used because of its efficiency in computation time and cost. However, improved quadrature schemes can be also considered [38].

All the examples consist of T-stress results obtained by means of the non-equilibrium formulation of the interaction integral method in conjunction with the FEM. In order to validate T-stress solutions, an inclined center crack in a homogeneous finite plate ($a/W = 0.1$) is investigated, and the FEM results are compared with analytical closed-form solutions. The same example is investigated for an FGM plate with exponentially graded material properties and compared with reference solutions obtained by means of the integral equation method by Paulino and Dong [65]. The second example investigates benchmark examples which have been used for laboratory experiments, and provides numerical solutions for T-stress and biaxiality ratio considering exponentially graded materials. The third example investigates the effect of scaling of FGM specimens on the T-stress and biaxiality ratio. The fourth example investigates an internal crack in an FGM strip. The fifth example consists of a slanted crack in a plate which was investigated by Eischen [17] and Kim and Paulino [23] who used the path-independent J_k^*-integral. The sixth example consists of an internal or an edge crack in a circular disk with exponentially graded material properties in the radial direction. The last example is provided to compare the present FEM results with experimental (static fracture test) results obtained by Marur and Tippur [69].

7.1. Inclined center crack in a plate

Fig. 12(a) and (b) show an inclined center crack of length $2a$ located with angle α (counter-clockwise) in a plate under constant traction and fixed-grip loading, respectively, Fig. 12(c) shows the complete mesh configuration, and Fig. 12(d) shows mesh detail using 12 sectors (S12) and 4 rings (R4) of elements around crack-tips. The displacement boundary condition is prescribed such that $u_2 = 0$ along the lower edge, and $u_1 = 0$ for the node at the left-hand side. The mesh discretization consists of 1641 Q8, 94 T6, and 24 T6qp elements, with a total of 1759 elements and 5336 nodes. The following data are used for the FEM analyses:

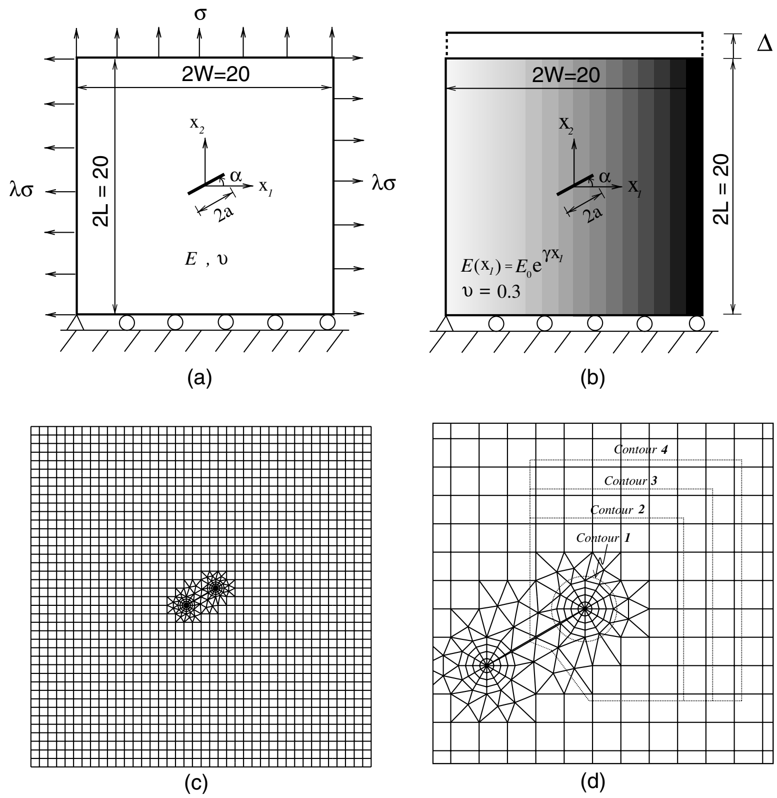

Fig. 12. Example 1: Plate with an inclined crack with angle α: (a) geometry and BCs for homogeneous case; (b) geometry and BCs for FGM case; (c) complete finite element mesh; (d) four different contours for the interaction integral and mesh detail using 12 sectors (S12) and 4 rings (R4) around the crack-tips ($\alpha = 30°$ counter-clockwise).

$$\begin{aligned}
&\text{plane stress, } 2 \times 2 \text{ Gauss quadrature,}\\
&a/W = 0.1, \quad L/W = 1.0,\\
&\alpha = (0° \text{ to } 90°).
\end{aligned}$$

7.1.1. Constant traction—homogeneous material case

This example has analytical solutions in which an inclined center crack in a homogeneous plate is subjected to far-field constant traction. The closed-form solutions are obtained by considering another large plate such that its edges are parallel or perpendicular to the crack, as shown in Fig. 13 [31]. The far-field stresses on the edges of the secondary boundary (see Fig. 13(b)) are

$$\sigma_{x_1x_1} = \sigma(\sin^2\alpha + \lambda\cos^2\alpha), \qquad \sigma_{x_2x_2} = \sigma(\cos^2\alpha + \lambda\sin^2\alpha), \qquad \sigma_{x_1x_2} = \sigma(1-\lambda)\sin\alpha\cos\alpha, \tag{54}$$

and the T-stress is given by [31]

$$T = \sigma(\lambda - 1)\cos 2\alpha. \tag{55}$$

The applied loads correspond to $\sigma_{22}(X_1, 10) = \sigma$ and $\sigma_{11}(\pm 10, X_2) = \lambda\sigma$, e.g. $\lambda = (0.0, 0.5)$ (see Fig. 12(a)). Young's modulus and Poisson's ratio are $E = 1.0$ and $\nu = 0.3$, respectively. Table 2 shows good agreement

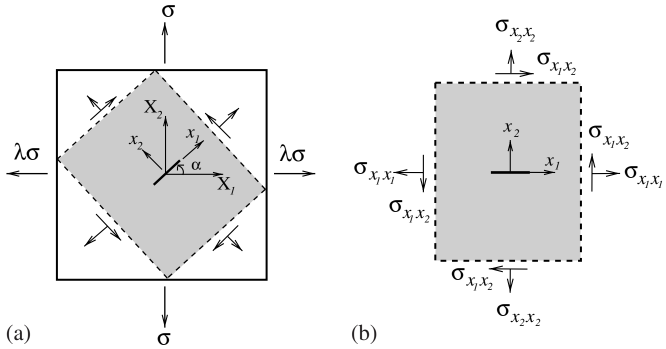

Fig. 13. Example 1: An inclined crack in a biaxially loaded homogeneous plate.

Table 2
Example 1: T-stress for an inclined center crack in a homogeneous plate under far-field constant traction (angle α: counter-clockwise). The exact solutions are obtained using Eq. (55). The parameter λ refers to the applied loading (see Figs. 12 and 13)

α (°)	$\lambda = 0.0$		$\lambda = 0.5$	
	Present	Exact	Present	Exact
0	−1.0070	−1.0000	−0.5089	−0.5000
15	−0.8738	−0.8660	−0.4434	−0.4330
30	−0.5083	−0.5000	−0.2612	−0.2500
45	−0.0073	0.0000	−0.0103	0.0000
60	0.4933	0.5000	0.2394	0.2500
75	0.8605	0.8660	0.4229	0.4330
90	0.9951	1.0000	0.4907	0.5000

between FEM results for T-stress obtained by the non-equilibrium formulation of the interaction integral method and the closed-form solution given by Eq. (55). For homogeneous materials, the results for T-stress for the right crack-tip are the same as those for the left crack-tip. This feature was observed in the FEM results obtained with the I-FRANC2D code. By comparing the data reported in Table 2, one observes that the numerical and analytical results agree quite well. For homogeneous materials, there is no difference in the results obtained using "non-equilibrium" and "incompatibility" [30] formulations.

7.1.2. Fixed-grip loading—FGM case

This example consists of an inclined center crack in an FGM plate subjected to fixed-grip loading. The applied load corresponds to $\sigma_{22}(X_1, 10) = \varepsilon_0 E_0 e^{\gamma X_1}$ (see Fig. 12(b)). This loading results in a uniform strain $\varepsilon_{22}(X_1, X_2) = \varepsilon_0$ in a corresponding uncracked structure. Young's modulus is an exponential function, i.e.

$$E(X_1) = E_0 e^{\gamma X_1}, \tag{56}$$

and the Poisson's ratio is taken as constant. The following data are used for the FEM analyses (consistent units):

$$\gamma a = (0 \text{ to } 0.5), \qquad E_0 = 1.0, \quad \nu = 0.3, \quad \varepsilon_0 = 1.0.$$

Table 3 compares the FEM results for T-stress obtained by the non-equilibrium formulation of the interaction integral method for various material non-homogeneity parameter γa with both those obtained

Table 3
Example 1: Comparison of T-stress for an inclined center crack in an FGM plate under fixed-grip loading (angle α: counter-clockwise). Notice that $\gamma a = 0.0$ refers to homogeneous material

Method	α (°)	$\gamma a = 0.00$		$\gamma a = 0.25$		$\gamma a = 0.50$	
		$T(+a)$	$T(-a)$	$T(+a)$	$T(-a)$	$T(+a)$	$T(-a)$
Non-equilibrium (present)	0	−0.9828	−0.9828	−0.9619	−0.9416	−0.8963	−0.8589
	15	−0.8534	−0.8534	−0.8338	−0.8179	−0.7734	−0.7478
	30	−0.4974	−0.4974	−0.4810	−0.4754	−0.4334	−0.4360
	45	−0.0055	−0.0055	−0.0067	−0.0023	0.0361	0.0115
	60	0.4912	0.4912	0.4987	0.4908	0.5133	0.4845
	75	0.8592	0.8592	0.8625	0.8567	0.8685	0.8502
	90	0.9950	0.9950	0.9949	0.9948	0.9945	0.9945
Incompatibility [30]	0	−0.9828	−0.9828	−0.9589	−0.9430	−0.8878	−0.8606
	15	−0.8534	−0.8534	−0.8310	−0.8191	−0.7655	−0.7494
	30	−0.4974	−0.4974	−0.4790	−0.4763	−0.4288	−0.4371
	45	−0.0055	−0.0055	−0.0077	−0.0019	0.0391	0.0109
	60	0.4912	0.4912	0.4992	0.4905	0.5146	0.4841
	75	0.8592	0.8592	0.8625	0.8569	0.8684	0.8505
	90	0.9950	0.9950	0.9949	0.9948	0.9946	0.9944
Paulino and Dong [65]	0	−0.9999	−0.9999	−0.9543	−0.9590	−0.8670	−0.8766
	15	−0.8660	−0.8660	−0.8266	−0.8316	−0.7483	−0.7631
	30	−0.5001	−0.5001	−0.4871	−0.4727	−0.4200	−0.4444
	45	0.0002	−0.0000	0.0106	0.0048	0.0393	0.0109
	60	0.4999	0.5000	0.5024	0.4981	0.5132	0.4905
	75	0.8660	0.8660	0.8665	0.8643	0.8701	0.8585
	90	1.0000	1.0000	1.0000	1.0000	1.0000	1.0000

by Paulino and Dong [65] using a singular integral equation method and FEM results obtained by Kim and Paulino [30] using the incompatibility formulation. Table 3 shows good agreement between FEM results for T-stress and the reference solutions. For homogeneous materials ($\gamma a = 0.0$), the results for T-stress for the right crack-tip are the same as those for the left crack-tip. This feature was captured by the I-FRANC2D code. Notice that as γa increases, T-stress for the right crack-tip ($T(+a)$) increases within the range of angle $0° \leqslant \alpha < 45°$ and $45° < \alpha < 90°$, however, T-stress for the left crack-tip ($T(-a)$) increases for the range of $0° \leqslant \alpha \leqslant 45°$, and then decreases for the range of $45° < \alpha < 90°$. The same trend in the results is observed by two very distinct methods, the FEM and the singular integral equation method.

Table 4 shows the breakdown of the J-integrals for the actual, auxiliary, superimposed fields, and the M-integral ($M = J^s - J - J^{aux}$) evaluated for the right tip of an inclined ($\alpha = 30°$) center crack under fixed-grip loading considering $\gamma a = 0.0$ (homogeneous material case) and $\gamma a = 0.5$. Four different contours are used as illustrated by Fig. 12(d). As expected, Table 4 shows path-independence of the M-integral as the domain becomes relatively large. We observe that, for homogeneous materials, there is a numerical remnant for J^{aux}, which theoretically should be zero. A similar observation has also been made by Kfouri [35] (see column for $J(f, t_0)$ in Table 1 of his paper). However, for FGMs, J^{aux} involves the non-equilibrium term (see Eq. (21)) for the non-equilibrium formulation or the incompatible term (see Eq. (A.1)) for the incompatibility formulation, and thus it is non-zero. Fig. 14 shows comparison of T-stress results obtained by including and neglecting the non-equilibrium term considering $\gamma a = 0.5$, $\alpha = 30°$ and four different contours as illustrated by Fig. 12(d). This plot clearly shows that in order to obtain converged solutions, the non-equilibrium term must be considered in the M-integral formulation. Notice that as the domain becomes large, the difference between the two solutions (including versus neglecting the non-equilibrium term) increases.

Table 4
Example 1: Breakdown of J-integrals for the actual, auxiliary, superimposed fields, and the M-integral ($M = J^s - J - J^{aux}$) for the calculation of T-stress at the right tip of an inclined center crack in a plate under fixed-grip loading ($\alpha = 30°$)

Formulation	γa	Contour	J^s	J	J^{aux}	M	T
Non-equilibrium and incompatibility	0.0	1	1.8305	2.3321	−0.00455	−0.4969	−0.4969
		2–4	1.8303	2.3307	−0.00223	−0.4974	−0.4974
Non-equilibrium	0.5	1	2.5137	2.8120	−0.01666	−0.2816	−0.4342
		2–4	2.5143	2.8110	−0.01556	−0.2811	−0.4334
Incompatibility	0.5	1	2.5013	2.8120	−0.03262	−0.2780	−0.4287
		2–4	2.5019	2.8110	−0.03100	−0.2781	−0.4288

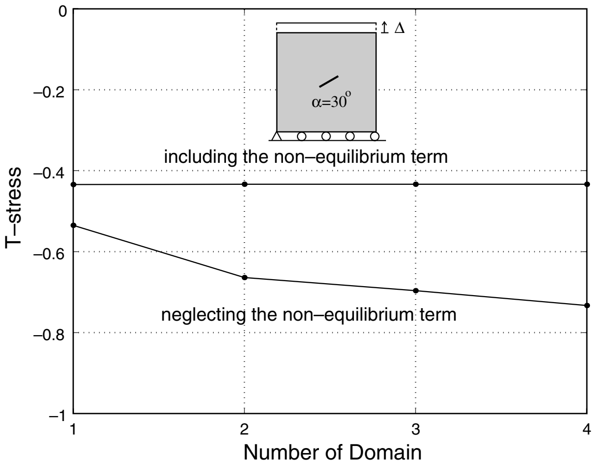

Fig. 14. Example 1: Comparison of T-stress obtained by either including or neglecting the non-equilibrium term (see Fig. 12(d) for the contours used).

7.2. Benchmark examples based on laboratory specimens

This example investigates the following benchmark laboratory specimens:

- single edge notched tension (SENT),
- double edge notched tension (DENT),
- center cracked tension (CCT),
- single edge notched bending (SENB),
- compact tension (CT).

A similar study for homogeneous materials was conducted by Sherry et al. [36]. They investigated two and three-dimensional cracked geometries, and provided T-stress and the biaxiality ratio for the above specimen types, but the dimensions are different from those considered in this paper. Fig. 15(a)–(e) show SENT, DENT, CCT, SENB, and CT specimens, respectively. Fig. 16(a)–(d) show the complete finite element meshes for SENT or SENB, DENT, CCT and CT specimens, respectively, and Fig. 16(e) shows the mesh detail of the CCT specimen using 12 sectors (S12) and 4 rings (R4) around the crack-tips. The applied loads are as follows:

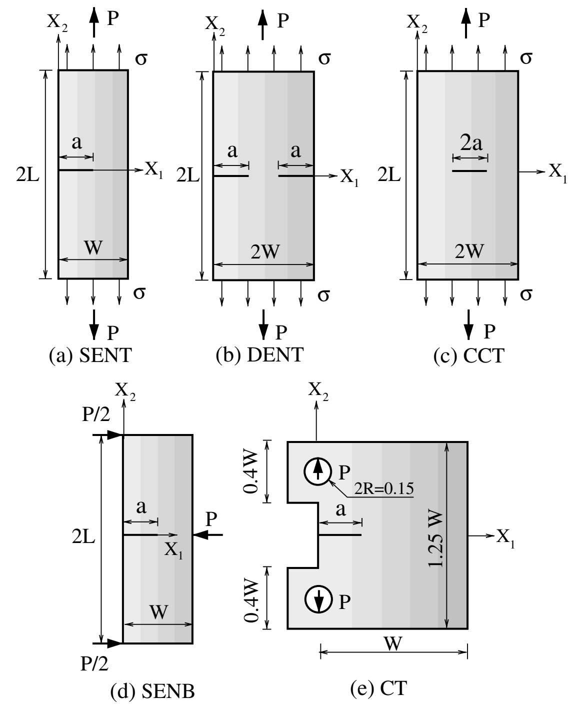

Fig. 15. Example 2: Laboratory specimens of thickness t: (a) single edge notched tension (SENT); (b) double edge notched tension (DENT); (c) center cracked tension (CCT); (d) single edge notched bending (SENB); (e) compact tension (CT). The load P is the point force for the SENB and CT specimens or the resultant for the equidistributed tractions (σ) on the boundary of the SENT, CCT, and DENT specimens.

$$\sigma_{22}(X_1, \pm L) = \sigma = 1 \quad \text{for SENT, DENT, and CCT,}$$

$$P(W, 0) = 1 \qquad \text{for SENB,}$$

$$P(0, \pm 0.275) = 1 \qquad \text{for CT,}$$

where σ_{22} is equidistributed traction on the boundary of FGM specimens.

The displacement boundary condition is prescribed as follows:

$$\begin{aligned}
&(u_1, u_2)(W, 0) = (0, 0), \quad u_2(a, 0) = 0 && \text{for SENT and CT,} \\
&(u_1, u_2)(a, 0) = (0, 0), \quad u_2(2W - a, 0) = 0 && \text{for DENT,} \\
&(u_1, u_2)(0, 0) = (0, 0), \quad u_2(2W, 0) = 0 && \text{for CCT,} \\
&(u_1, u_2)(0, L) = (0, 0), \quad u_1(0, -L) = 0 && \text{for SENB.}
\end{aligned} \tag{57}$$

Young's modulus is an exponential function given by

$$E(X_1) = E_1 e^{\gamma X_1}, \tag{58}$$

where $E_1 = E(0)$ and $E_2 = E(W)$ for SENT, SENB, and CT specimens and $E_1 = E(0)$ and $E_2 = E(2W)$ for DENT and CCT specimens. The Poisson's ratio is taken as constant for all the specimens. The following data are used for the FEM analyses (consistent units):

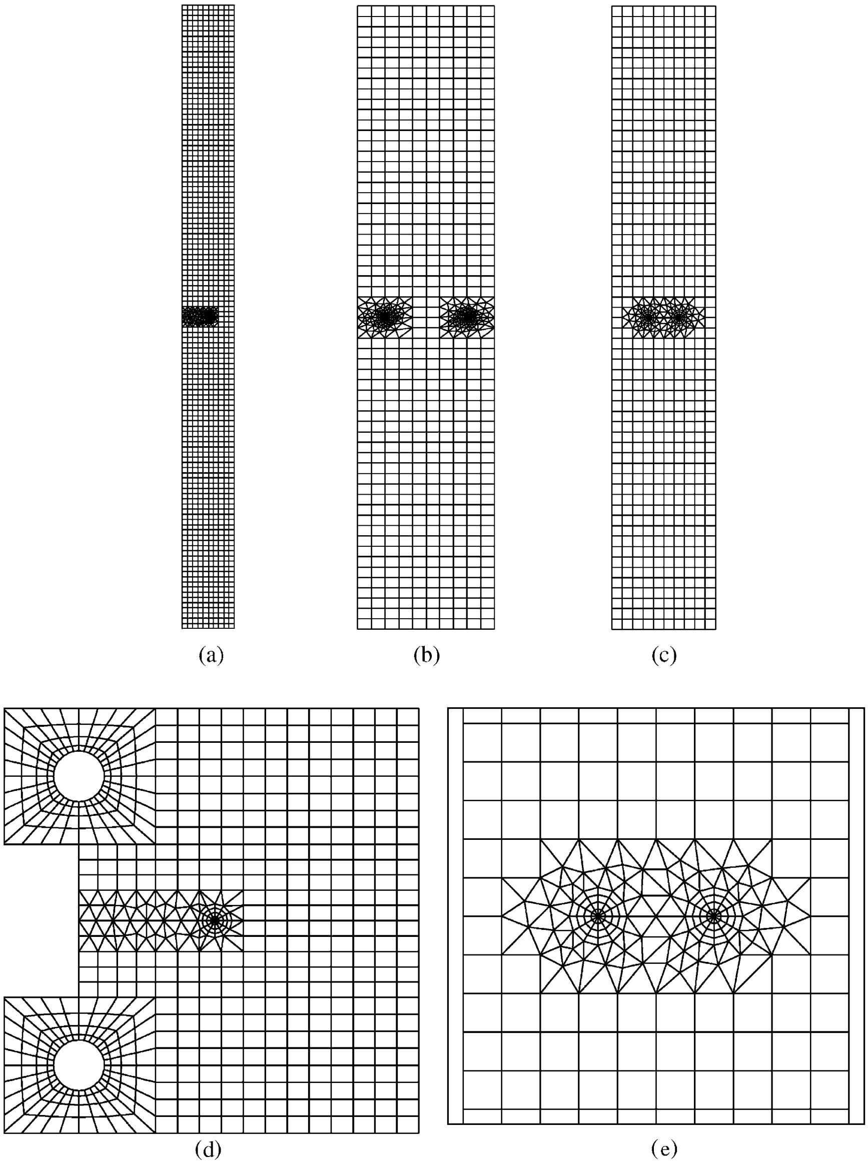

Fig. 16. Example 2: Finite element meshes: (a) single edge notched tension (SENT) and single edge notched bending (SENB); (b) double edge notched tension (DENT); (c) center cracked tension (CCT); (d) compact tension (CT); (e) mesh detail of the CCT specimen using 12 sectors (S12) and 4 rings (R4) around the crack-tips.

$$\begin{aligned} &\text{plane strain, } 2 \times 2 \text{ Gauss quadrature,} \\ &a/W = (0.1 \text{ to } 0.8), \quad L = 6.0, \quad W = 1.0, \\ &E_2/E_1 = (0.1, 0.2, 1.0, 5, 10), \\ &E_1 = 1.0, \quad \nu = 0.3. \end{aligned} \tag{59}$$

Fig. 17 shows the biaxiality ratio ($\beta = T\sqrt{\pi a}/K_{\mathrm{I}}$) versus the ratio of crack length to width a/W for various specimens considering homogeneous materials ($E_2 = E_1$). The mode I SIF K_{I} is calculated by the

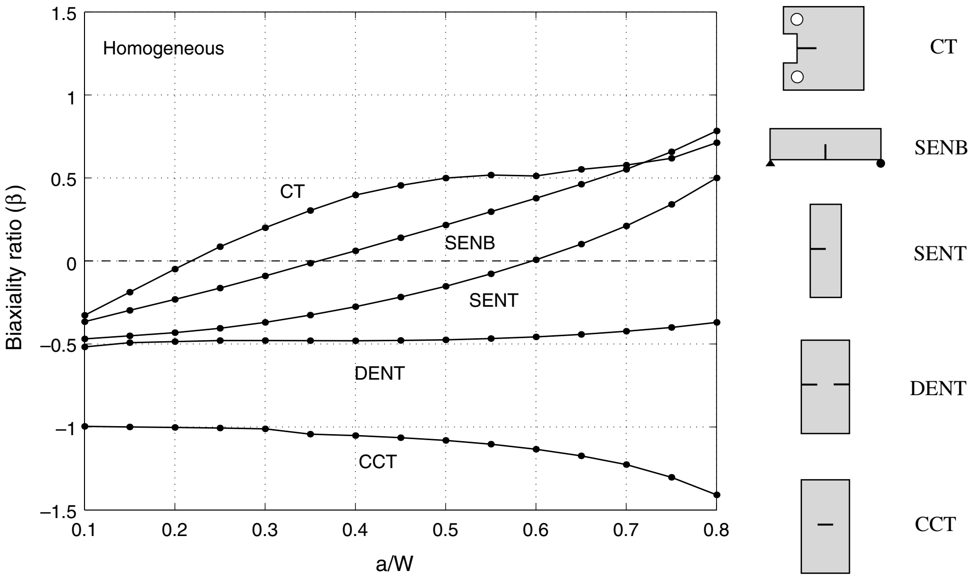

Fig. 17. Example 2: Biaxiality ratio ($\beta = T\sqrt{\pi a}/K_I$) for a homogeneous material ($E_1 = E_2$).

non-equilibrium formulation of the interaction integral method using appropriate auxiliary fields for SIFs [70]. The auxiliary fields consist of Williams's asymptotic displacement and strain fields, and stress fields constructed by Eq. (9). Notice that the sign of biaxiality ratio changes from negative to positive as the ratio of crack length to width (a/W) is about 0.22 for CT, 0.35 for SENB, and 0.60 for SENT specimen, however, it remains negative for DENT and CCT specimens. Fig. 18 shows biaxiality ratio ($\beta = T\sqrt{\pi a}/K_I$) versus a/W for various specimens considering exponentially graded materials with $E_2/E_1 = 10$. For the CCT and DENT specimens, which have two crack-tips, the biaxiality ratio is calculated for the right crack-tip. By comparing Figs. 17 and 18, we observe that the transition point of the sign of biaxiality ratio shifts to the left due to the material gradation in the CT, SENB, and SENT specimens. Moreover, the behavior of the biaxiality ratio for CCT and DENT is significantly different from that for a homogeneous material.

The T-stress and biaxiality ratio are evaluated for all the specimens considering various ratios of E_2/E_1. Fig. 19 shows the biaxiality ratio ($\beta = T\sqrt{\pi a}/K_I$) versus a/W for the SENT specimen. The transition point of the sign of biaxiality ratio shifts to the left as E_2/E_1 increases. For a fixed value of a/W considered here, the biaxiality ratio ($\beta = T\sqrt{\pi a}/K_I$) increases with increasing E_2/E_1. Fig. 20 shows the biaxiality ratio ($\beta = T\sqrt{\pi a}/K_I$) versus a/W for the DENT specimen. For the range of a/W between 0.1 and 0.75, the T-stress and biaxiality ratio are negative. For $E_2/E_1 = 0.1$, as the ratio a/W increases from 0.75 to 0.8, the biaxiality ratio becomes positive. For a fixed value of a/W considered here, the biaxiality ratio decreases with increasing E_2/E_1. Fig. 21 shows biaxiality ratio ($\beta = T\sqrt{\pi a}/K_I$) versus a/W for the CCT specimen. For the range of a/W considered, the T-stress and biaxiality ratio are negative. For a fixed value of a/W, the biaxiality ratio ($\beta = T\sqrt{\pi a}/K_I$) increases with increasing E_2/E_1. Fig. 22 shows the biaxiality ratio versus a/W for the SENB specimen. The transition point of the sign of biaxiality ratio shifts to the left as E_2/E_1 increases. For a fixed value of a/W considered here, the biaxiality ratio increases with increasing E_2/E_1. Fig. 23 shows biaxiality ratio ($\beta = T\sqrt{\pi a}/K_I$) versus a/W for the CT specimen. The transition point of the sign of biaxiality ratio shifts to the left as E_2/E_1 increases. For a fixed value of a/W, the biaxiality ratio increases with increasing E_2/E_1. Based on the above investigations, we observe that the material gradation (represented by the ratio E_2/E_1) significantly influences the T-stress and biaxiality ratio for all the specimens considered.

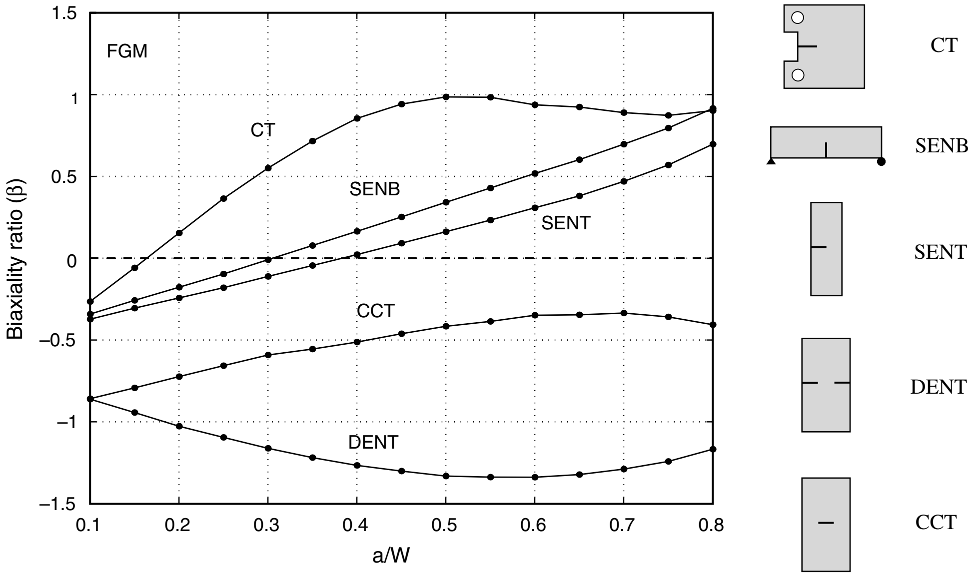

Fig. 18. Example 2: Biaxiality ratio ($\beta = T\sqrt{\pi a}/K_I$) for an FGM considering $E_2/E_1 = 10$. For center cracked tension (CCT) and double edge notched tension (DENT) specimens, the biaxiality ratio is evaluated at the right crack-tip.

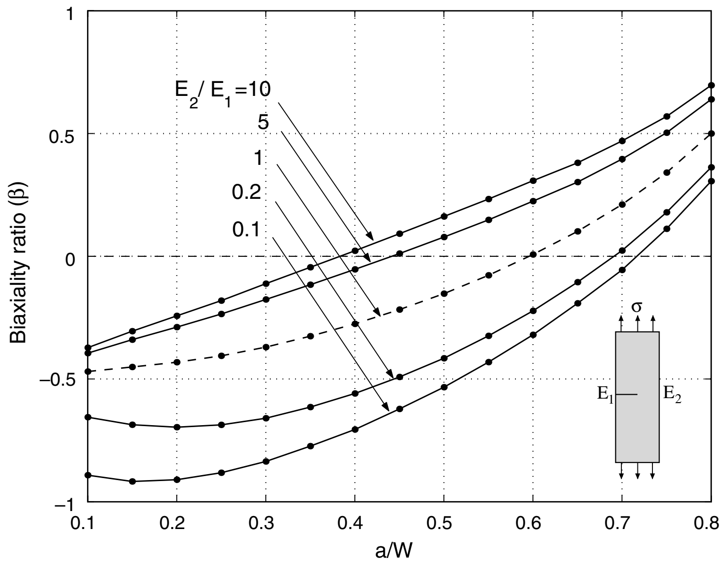

Fig. 19. Example 2: Biaxiality ratio ($\beta = T\sqrt{\pi a}/K_I$) for the single edge notched tension (SENT) specimen (see Fig. 15(a)).

For graded laboratory specimens, the mode I SIF (K_I) is associated with material non-homogeneity, and it can be given by

$$K_I = \frac{P}{t\sqrt{W}} f\left(\frac{a}{W}, \gamma\right), \tag{60}$$

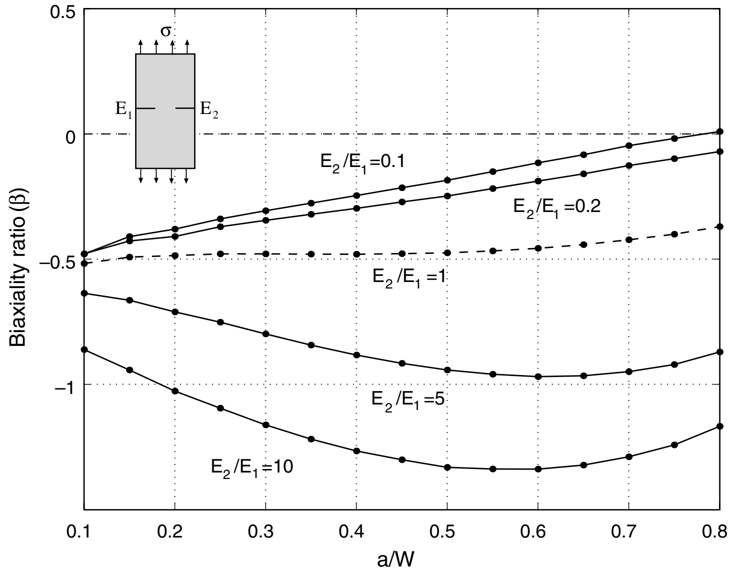

Fig. 20. Example 2: Biaxiality ratio ($\beta = T\sqrt{\pi a}/K_{\mathrm{I}}$) evaluated at the right crack-tip for the double edge notched tension (DENT) specimen.

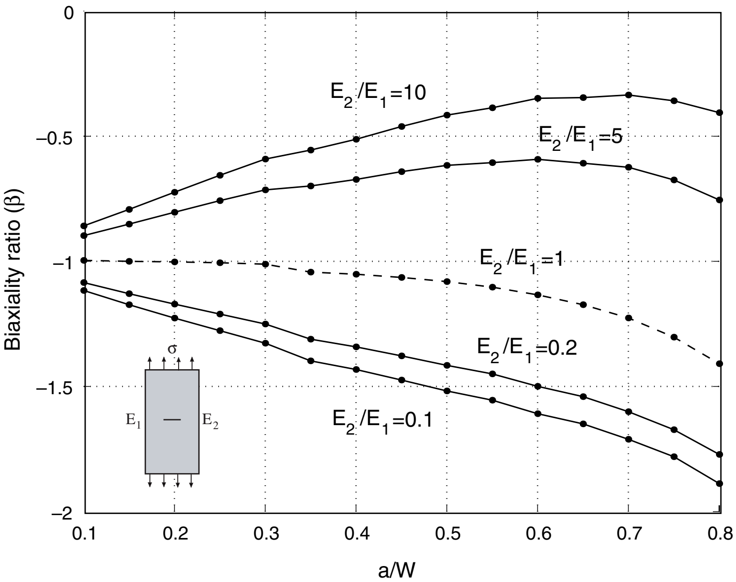

Fig. 21. Example 2: Biaxiality ratio ($\beta = T\sqrt{\pi a}/K_{\mathrm{I}}$) evaluated at the right crack-tip for the center cracked tension (CCT) specimen.

where t is the thickness of the specimen, and P is either the point force for the SENB and CT specimens or the resultant for the equidistributed tractions (σ) on the boundary of the SENT, CCT, DENT specimens (see Fig. 15). For homogeneous specimens [20], $\gamma = 0$ (there is no effect of non-homogeneity). Using Eq. (2), one obtains

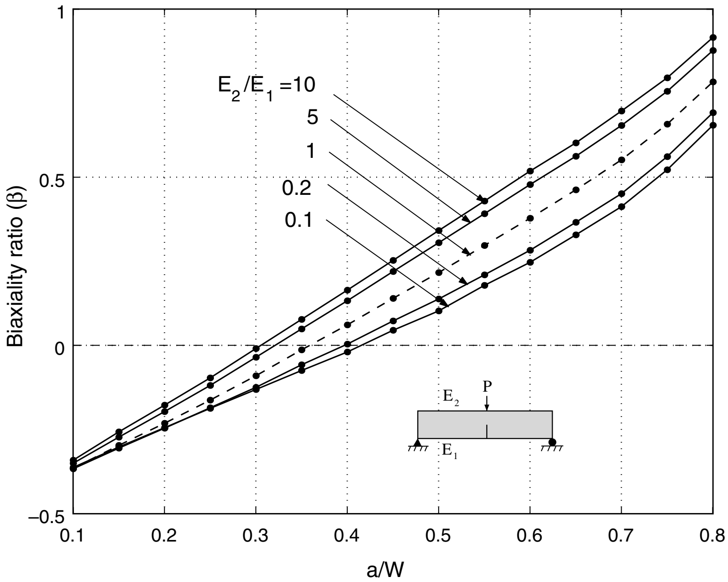

Fig. 22. Example 2: Biaxiality ratio ($\beta = T\sqrt{\pi a}/K_{\mathrm{I}}$) for the single edge notched bending (SENB) specimen (see Fig. 15(b)).

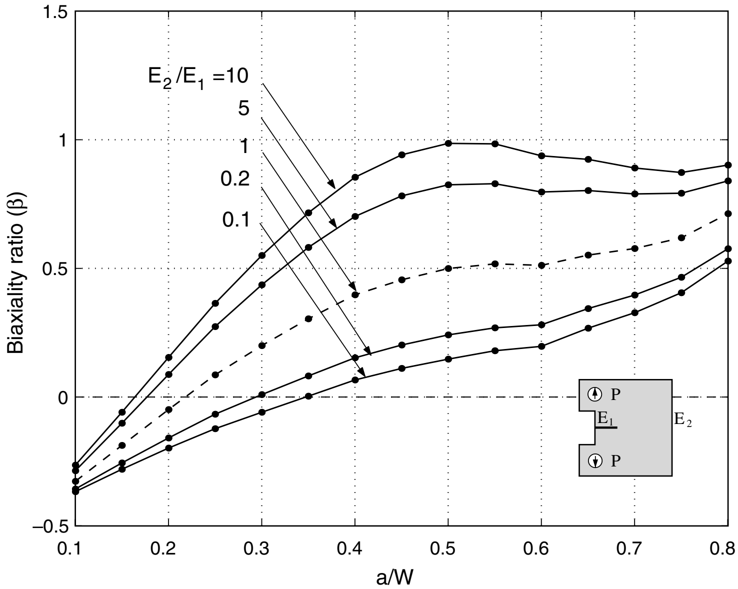

Fig. 23. Example 2: Biaxiality ratio ($\beta = T\sqrt{\pi a}/K_{\mathrm{I}}$) for the compact tension (CT) specimen.

$$T = \frac{\beta P}{t\sqrt{\pi a W}} f\left(\frac{a}{W}, \gamma\right). \tag{61}$$

Notice that the T-stress is also a function of the material non-homogeneity parameter γ.

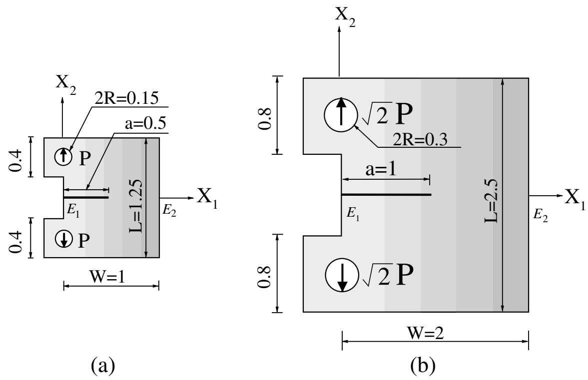

Fig. 24. Example 3: Two graded compact tension (CT) specimens with $a/W = 0.5$: (a) specimen A; (b) specimen B, which is two times as large as specimen A. For both specimens, J is the same, and the Young's modulus varies along the X_1 direction from E_1 on the left to E_2 on the right-hand-side.

7.3. On scaling of FGM specimens

This section investigates the effect of scaling of FGM specimens on the T-stress and biaxiality ratio. Here we consider the compact tension (CT) specimen with a fixed a/W ratio and two geometries where one is twice as large as the other. The loads are applied considering a given value of J (or K_{I}). Fig. 24(a) and (b) show the geometry and BCs for the two specimens A and B, respectively. Fig. 16(d) shows the complete finite element mesh adopted for these two CT specimens. For the large specimen (B) to have the same K_{I} as that for the small specimen (A), the applied load to specimen B should be $\sqrt{2}P$ (see Eq. (60)).

The Young's modulus is taken as an exponential function given by

$$E(X_1) = E_1 e^{\gamma X_1}, \tag{62}$$

where $E_1 = E(0)$, however, the present argument is independent of the specific material variation considered. Notice that as $\gamma = \log[E(W)/E(0)]/W$, the non-homogeneity parameter γ_{B} for specimen B is half of γ_{A} for specimen A. Thus, for both specimens in Fig. 24 $E_2 = E(W) = E_1 e^{\gamma_{\mathrm{A}} W}$. The Poisson's ratio is taken as constant for the two specimens.

For these specific relations of non-homogeneity parameters, i.e. $\gamma_{\mathrm{A}} = 2\gamma_{\mathrm{B}}$, the biaxiality ratio remains unchanged. Using

$$T = \beta \frac{K_{\mathrm{I}}}{\sqrt{\pi a}}, \tag{63}$$

one observes that T-stress is proportional to $1/\sqrt{a}$. Thus

$$T_{\mathrm{A}} = \sqrt{2} T_{\mathrm{B}}, \tag{64}$$

where T_{A} and T_{B} denotes the T-stress for specimens A (small) and B (large), respectively.

This theoretical argument is also observed in the numerical calculation. The following data are used for the FEM analyses (consistent units):

$$\begin{aligned}&\text{plane strain}, \; 2\times 2 \text{ Gauss quadrature},\\ &a/W = 0.5, \quad W = 1.0, 2.0,\\ &E_2/E_1 = 10,\\ &E_1 = 1.0, \quad \nu = 0.3, \quad P = 1.\end{aligned} \tag{65}$$

For specimen A, the mode I SIF (K_I), T-stress, biaxiality ratio are obtained as (cf. Fig. 23)

$$(K_I)_A = 7.130, \qquad T_A = 5.607, \qquad \beta_A = 0.985. \tag{66}$$

For specimen B, the mode I SIF (K_I), T-stress, biaxiality ratio are obtained as (cf. Fig. 23)

$$(K_I)_B = 7.130, \qquad T_B = 3.964, \qquad \beta_B = 0.985. \tag{67}$$

Notice that, numerically, $T_A/T_B = 1.4144$, which is very close to $\sqrt{2}$. Therefore the biaxiality ratio plays an important role as a non-dimensional parameter not only for homogeneous materials and but also for FGMs.

7.4. Internal crack in a strip

Fig. 25(a) and (b) show geometry and boundary conditions (BCs) used in the present FEM analysis and the singular integral equation (SIE) method used by Paulino and Dong [65], respectively, for an internal crack in an FGM strip. Fig. 25(c) shows complete mesh discretization and Fig. 25(d) shows mesh detail using 12 sectors (S12) and 4 rings (R4) of elements around crack-tips. The displacement boundary condition is prescribed such that $u_1 = u_2 = 0$ for the center node on the left edge, and $u_2 = 0$ for the center node on the right edge. For the present FEM analyses, the applied load is prescribed on the upper and lower edges with normal stress $\sigma_{22}(-W \leqslant X_1 \leqslant W, \pm h) = \varepsilon_0 E_0 e^{\gamma X_1}$, and for the SIE approach, Paulino and Dong [65] applied the load on the upper and lower crack faces with normal stress $\sigma_{22}(-a \leqslant X_1 \leqslant a, \pm 0) = \varepsilon_0 E_0 e^{\gamma X_1}$. These loads lead to the same SIF and T-stress.

Young's modulus is an exponential function, i.e.

$$E(X_1) = E_0 e^{\gamma X_1}, \tag{68}$$

and the Poisson's ratio is taken as constant. The mesh discretization consists of 1050 Q8, 209 T6, and 24 T6qp elements, with a total of 1283 elements and 3856 nodes. The following data are used for the FEM analyses (consistent units):

$$\begin{aligned}&\text{plane strain}, \; 2\times 2 \text{ Gauss quadrature},\\ &a/W = 0.1, \quad W = 10, \quad h = 1,\\ &\gamma a = (0, 0.25, 0.50),\\ &E_1 = 1.0, \quad \nu = 0.3, \quad \varepsilon_0 = 1.0.\end{aligned} \tag{69}$$

Table 5 compares T-stress obtained by the non-equilibrium formulation of the interaction integral method with that obtained by Paulino and Dong [65] using the SIE method. The FEM results for T-stress agree reasonably well with corresponding reference results. Notice that Paulino and Dong [65] used $\gamma a = 0.001$ for the homogeneous case, and mode I SIF and T-stress for the right crack-tip are different from those for the left crack-tip.

7.5. Slanted edge crack in a plate

Fig. 26(a) shows a slanted edge crack in a plate, Fig. 25(b) shows the coarse mesh discretization using (S8, R2) at the crack-tip region, which is the same as the one used by Eischen [17] and Kim and Paulino

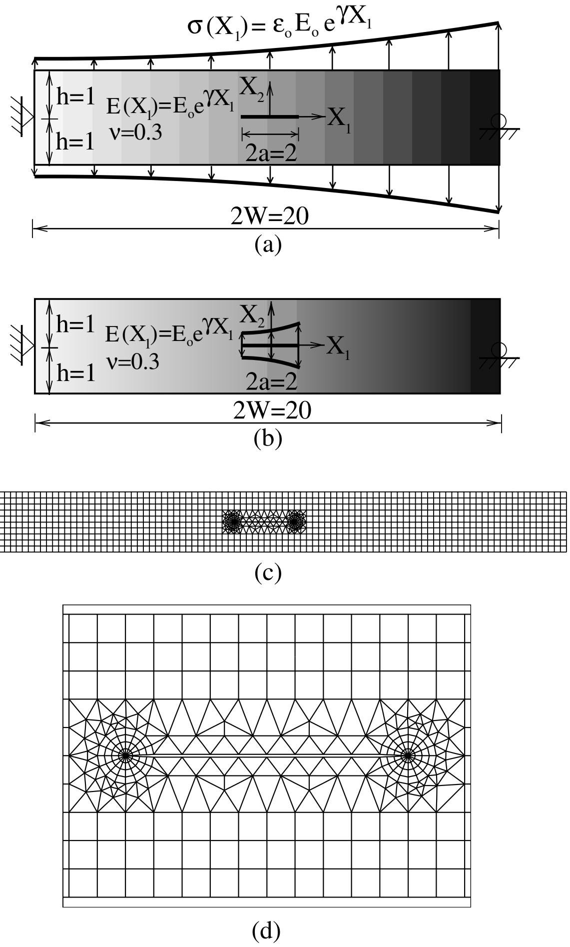

Fig. 25. Example 4: An internal crack in an FGM strip: (a) geometry and BCs used for the FEM; (b) geometry and BCs used for the singular integral equation (SIE) method [65]; (c) complete finite element mesh; (d) mesh detail using 12 sectors (S12) and 4 rings (R4) around the crack-tips.

Table 5
Example 4: T-stress for an internal crack in strip. Paulino and Dong [65] used $\gamma a = 0.001$ for the homogeneous case

γa	Present (FEM)				SIE [65]			
	K_I^+	K_I^-	T^+	T^-	K_I^+	K_I^-	T^+	T^-
0.00	1.8234	1.8234	−0.8989	−0.8989	1.8167	1.8143	−0.9431	−0.9447
0.25	2.1484	1.5408	−0.6586	−1.0571	2.1391	1.5352	−0.6913	−1.1087
0.50	2.5224	1.2959	−0.3325	−1.1410	2.5120	1.2923	−0.3450	−1.1950

[23], and Fig. 26(c) shows the refined mesh discretization using (S12, R4) at the crack-tip region. The applied load is prescribed on the upper edge with normal stress $\sigma_{22}(X_1, 1) = \varepsilon_0 E_0 e^{\gamma(X_1 - 0.5)}$. The displacement boundary condition is specified such that $u_2 = 0$ along the lower edge, and $u_1 = 0$ for the node at the right hand side.

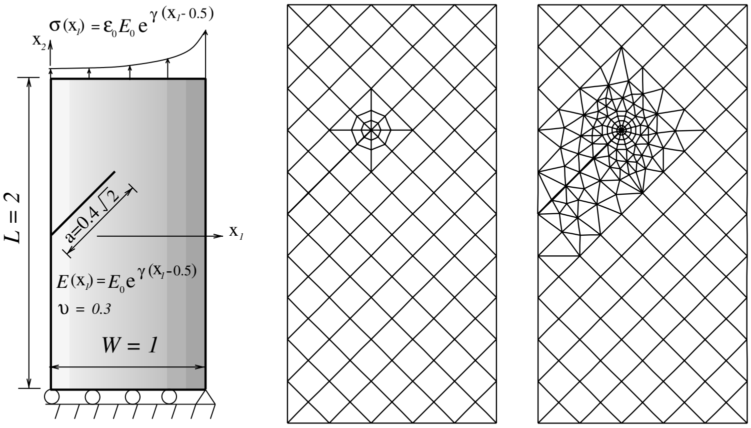

(a) (b) (c)

Fig. 26. Example 5: Slanted edge crack in a plate; (a) geometry and BCs; (b) coarse FEM mesh using (S8, R2) at the crack-tip, which is the same mesh used by Eischen [17]; (c) refined FEM mesh using (S12, R4) at the crack-tip.

Young's modulus is an exponential function, i.e.

$$E(X_1) = E_0 \mathrm{e}^{\gamma(X_1-0.5)}, \tag{70}$$

and the Poisson's ratio is taken as constant. The coarse mesh has 97 Q8, 30 T6, and 8 T6qp with a total of 135 elements and 412 nodes; and the refined mesh has 126 Q8, 145 T6, and 12 T6qp elements, with a total of 283 elements and 714 nodes. The following data are used for the FEM analyses (consistent units):

$$\begin{aligned} &\text{plane strain}, \ 2 \times 2 \ \text{Gauss quadrature}, \\ &a/W = 0.4\sqrt{2}, \quad L/W = 2.0, \\ &\gamma a = (0 \ \text{to} \ 0.40\sqrt{2}), \\ &E_1 = 1.0, \quad v = 0.3, \quad \varepsilon_0 = 1.0. \end{aligned} \tag{71}$$

Table 6 shows a comparison of T-stress obtained by the non-equilibrium formulation of the interaction integral method using the coarse mesh (S8, R2) shown in Fig. 26(b) in comparison with those obtained by Kim and Paulino [23] (using the J_k^*-integral EDI) and Eischen [17] (using the J_k^* contour integral). It also shows comparison of T-stress obtained by the present method using the refined mesh (S12, R4) shown in Fig. 26(c) in comparison with the results obtained by means of the J_k^*-integral (EDI) [23]. The T-stress

Table 6
Example 5: T-stress for a slanted edge crack in a plate using (S8, R2) and (S12, R4) for the crack-tip region discretization

Discretization	(S8, R2)			(S12, R4)	
γa	Present	Kim and Paulino [23]	Eischen [17]	Present	J_k^*-integral [23]
0.00	0.747	0.796	0.822	0.764	0.787
$0.04\sqrt{2}$	0.720	0.769	–	0.737	0.760
$0.10\sqrt{2}$	0.682	0.731	–	0.698	0.722
$0.20\sqrt{2}$	0.625	0.673	–	0.641	0.663
$0.30\sqrt{2}$	0.574	0.620	–	0.589	0.611
$0.40\sqrt{2}$	0.529	0.572	0.588	0.544	0.564

results in Table 6 indicate reasonable agreement between the present numerical results and corresponding reference results.

7.6. Internal or edge crack in a circular disk

This example considers two crack geometries, i.e. internal and edge cracks. Fig. 27(a) and (b) show geometry and boundary conditions for internal and edge cracks, respectively. Three different loadings are considered, i.e. constant normal traction, point tensile load, and point compressive load. The applied loads correspond to $\sigma_n = 1.0$ for constant normal traction, and $P = 1.0$ for point (tensile and compressive) loads. The displacement boundary condition is prescribed such that $(u_1, u_2) = (0, 0)$ for the node at $(X_1, X_2) = (R, 0)$ and $u_2 = 0$ for the node at $(X_1, X_2) = (-R, 0)$ for an internal center crack, and such that $(u_1, u_2) = (0, 0)$ for the node at $(X_1, X_2) = (R, 0)$ and $u_2 = 0$ at the crack-tip node for an edge crack.

Young's modulus is an exponential function of the radius r given by

$$E(r) = E_0 \mathrm{e}^{\gamma r}, \tag{72}$$

and its derivatives are given by

$$\frac{\partial E(r)}{\partial X_1} = \frac{\partial E(r)}{\partial r}\frac{\partial r}{\partial X_1} = (\gamma \cos\alpha) E_0 \mathrm{e}^{\gamma r}, \qquad \frac{\partial E(r)}{\partial X_2} = \frac{\partial E(r)}{\partial r}\frac{\partial r}{\partial X_2} = (\gamma \sin\alpha) E_0 \mathrm{e}^{\gamma r}. \tag{73}$$

Eqs. (72) and (73) are used in the interaction integral method, which involves the constitutive tensors **C** and its derivatives. The following data are used for the FEM analyses (consistent units):

plane strain, 2×2 Gauss quadrature,

$\omega = a/R = 0.1, 0.2$ for an internal crack,

$\omega = a/(2R) = 0.1, 0.2$ for an edge crack,

$\gamma = (-1.0, -0.5, 0.0, 0.5, 1.0)$,

$E_0 = 1.0, \quad \nu = 0.3, \quad R = 2.0.$

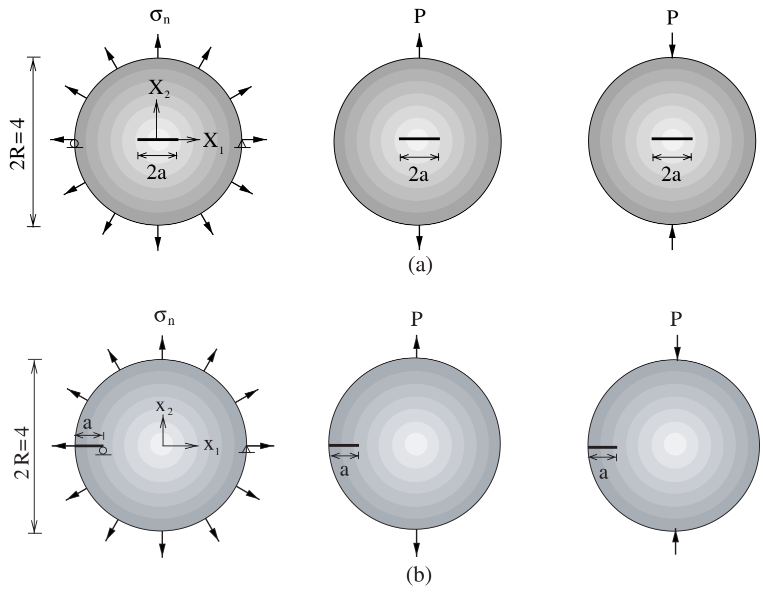

Fig. 27. Example 6: Geometry and BCs: (a) internal crack in a circular disk; (b) edge crack in a circular disk.

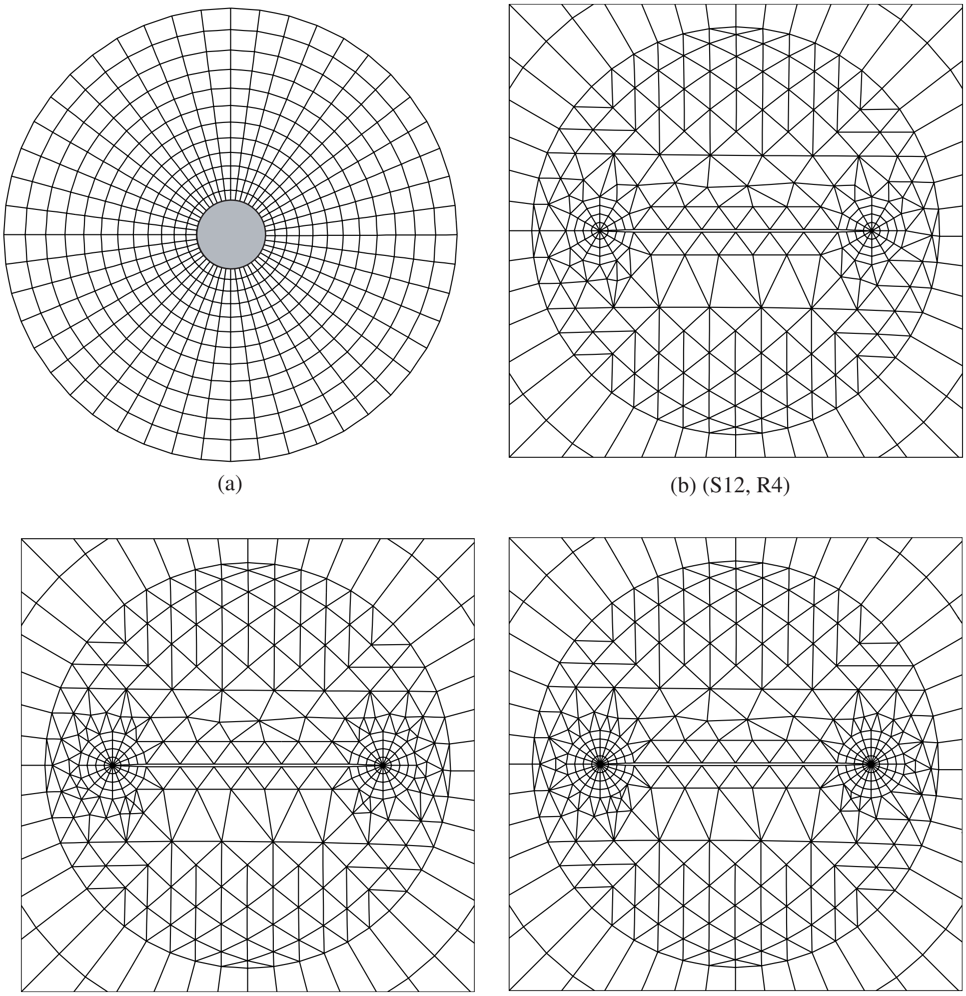

(a) (b) (S12, R4)

(c) (S16, R4) (d) (S20, R4)

Fig. 28. Example 6: Sensitivity of crack-tip discretization on the accuracy of T-stress: (a) partial FEM mesh configuration with the shaded region indicating the location where a mesh refinement study is conducted; (b) twenty sectors (S12); (c) sixteen sectors (S16); (d) twenty sectors (S20). Four rings (R4) of elements are used along the radial direction for all three cases.

Here we investigate the sensitivity of mesh discretization on the accuracy of T-stress by increasing the number of sectors around the crack-tip, i.e. S12, S16, and S20. Fig. 28(a) shows the partial FEM mesh for the internal crack in a disk in which the shaded region indicates the location where various mesh discretizations are applied. Fig. 28(b)–(d) illustrate mesh details using 12 sectors (S12), 16 sectors (S16), and 20 sectors (S20), respectively. Table 7 provides the mesh statistics for each case. Four rings (R4) of elements are used along the radial direction for all three cases. Table 8 shows the influence of crack-tip discretization on the accuracy of the T-stress considering S12, S16, and S20 sectors for the internal crack in a disk subjected to the tension point load. According to Table 8, improved mesh refinement around the crack-tips increases accuracy of the T-stress results.

Based on the sensitivity study, we use the crack-tip template with S20 sectors (S20) and 4 rings (R4) for the examples investigated in this section. Table 9 shows the FEM results for the T-stress for an internal

Table 7
Example 6: Mesh discretization using three crack-tip templates

Mesh	Crack-tip templates		
	(S12, R4)	(S16, R4)	(S20, R4)
Q8	441	659	686
T6	290	368	361
T6qp	24	32	40
Elements	755	1059	1087
Nodes	2048	2864	2944

Table 8
Example 6: Sensitivity of crack-tip discretization on the accuracy of T-stress for an internal crack in a circular disk (see Fig. 28). Four rings (R4) of elements are used along the radial direction for all three cases, i.e. S12, S16, and S20

Loading	ω	Sectors			Fett [72]
		S12	S16	S20	
P (tens.)	0.1	−0.6294	−0.6281	−0.6266	−0.6257

Table 9
Example 6: T-stress for an internal crack in a circular disk considering the (S20, R4) crack-tip template (see Figs. 27(a) and 28(a and d))

Loading	ω	$\gamma = 0.0$		$\gamma = -1.0$	$\gamma = -0.5$	$\gamma = 0.5$	$\gamma = 1.0$
		Present	Fett [72]				
σ_n	0.1	−0.0228	−0.0216	−0.2292	−0.1115	0.0322	0.0585
	0.2	−0.0795	−0.0805	−0.4549	−0.2412	0.0244	0.0789
P (tens.)	0.1	−0.6266	−0.6257	−0.8508	−0.7271	−0.5070	−0.3912
	0.2	−0.6003	−0.5983	−0.8818	−0.7269	−0.4802	−0.3768

crack considering the (S20, R4) crack-tip template. For a homogeneous material ($\gamma = 0.0$), the results for the T-stress show relatively good agreement with those obtained by Fett [71–73] who used the boundary collocation method. As γ increases, the T-stress increases for constant normal traction and point tension load. As expected, the T-stress for point tension load changes sign in comparison with the T-stress for point compression load, while the magnitude is the same on both cases.

Fig. 29(a) shows the complete FEM mesh discretization for an edge crack in a circular disk, and Fig. 29(b) shows the mesh detail using the (S20, R4) crack-tip template discussed above. Table 10 shows the FEM results for T-stress for an edge crack in a circular disk. As γ increases, the T-stress decreases for constant normal traction and point tension load. For the point compression load, the values of T-stress change sign compared to those for the point tension load, while the magnitude is the same on both cases.

7.7. Three-point bending specimen with crack perpendicular to material gradation

This example is based on the experimental investigation by Marur and Tippur [74], who have fabricated FGM specimens using gravity assisted casting technique with two-part slow curing epoxy and uncoated solid glass sphere fillers. Fig. 30(a) shows specimen geometry and BCs, Fig. 30(b) shows the complete mesh configuration, and Fig. 30(c) shows mesh detail using 12 sectors (S12) and 4 rings (R4) around the crack-tip. Here we consider the material properties used in the experiments [74] and also small perturbations on the Young's modulus. Fig. 31 illustrates four different linear variations of Young's modulus $E(X_1)$ in the

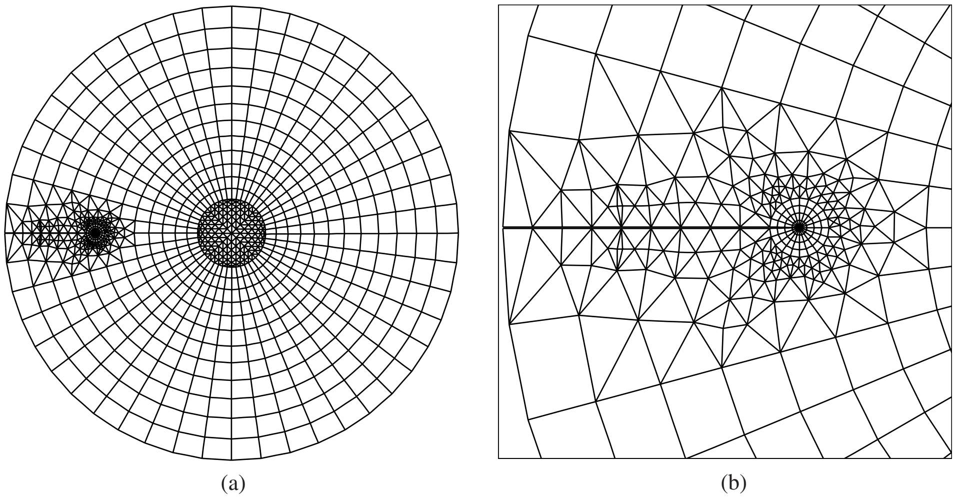

Fig. 29. Example 6: An edge crack in a circular disk: (a) the complete mesh configuration; (b) mesh detail using 20 sectors (S20) and 4 rings (R4) around the crack-tip.

Table 10
Example 6: T-stress for an edge crack in a circular disk considering the (S20, R4) crack-tip template (see Figs. 27(b) and 29(a and b))

Loading	ω	$\gamma = 0.0$		$\gamma = -1.0$	$\gamma = -0.5$	$\gamma = 0.5$	$\gamma = 1.0$
		Present	Fett [73]				
σ_n	0.1	0.5812	0.5853	0.9718	0.7930	0.2619	−0.1428
	0.2	0.7365	0.7407	1.4836	1.1389	0.2321	−0.3748
P (tens.)	0.1	−0.0718	−0.0714	−0.0314	−0.0471	−0.1061	−0.1544
	0.2	−0.1830	−0.1819	−0.0801	−0.1257	−0.2602	−0.3600

graded material region and a fixed linear variation of Poisson's ratio $\nu(X_1)$. The numerical values of the material properties at the end points of the gradation region are given in Table 11.

The mesh discretization consists of 1891 Q8, 199 T6, and 12 T6qp elements, with a total of 2102 elements and 6341 nodes. The following data are used for the FEM analyses:

$$\begin{aligned}&\text{plane strain},\ 2\times 2 \text{ Gauss quadrature},\\ &a = 6.6 \text{ mm},\quad t = 6.8 \text{ mm},\quad P = 100 \text{ N}.\end{aligned} \tag{74}$$

For the material variation $E(X_1)$ in the range [3.490–10.790] GPa, Marur and Tippur [74] used the experimental strain data and computed $|\mathbf{K}| = 0.65$ MPa $\sqrt{\text{m}}$ and $\psi = -3.45°$, while their numerical (FEM) results are $|\mathbf{K}| = 0.59$ MPa $\sqrt{\text{m}}$ and $\psi = -3.24°$, where $\psi = \tan^{-1}(K_{\text{II}}/K_{\text{I}})$ is the mode-mixity parameter.

Table 12 shows T-stress and SIFs obtained by the non-equilibrium formulation of the interaction integral method for four different material variations and also compares SIFs with those obtained by Marur and Tippur [74] for the specific material variation, $E(X_1)$, [3.490–10.790] GPa. Notice that, as the slope of material variation becomes steeper, both T-stress and SIFs decrease, and the absolute value of the phase angle ψ increases.

To further compare the present results for SIFs and mode-mixity with other available reference results, Table 13 shows the results obtained by the M-integral, the results by three different methods (modified crack closure, J_k^*-integral, and displacement correlation technique) reported by Kim and Paulino [23], and

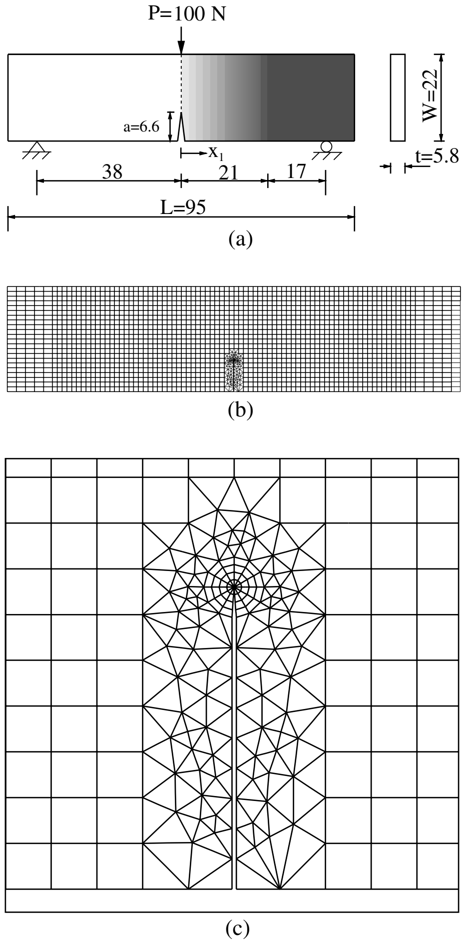

Fig. 30. Example 7: Three-point bending specimen with a crack perpendicular to the material gradation: (a) geometry and BCs (Units:N, mm); (b) the complete mesh configuration; (c) mesh detail using 12 sectors (S12) and 4 rings (R4) around the crack-tip.

also the results obtained numerically and experimentally by Marur and Tippur [74] for Case 2 ($E = 3.490$ to 10.790 GPa) of Table 12. There are differences in the results for SIFs and mode-mixity obtained by the present approach (M-integral) and those by Marur and Tippur [74]. While we cannot comment on their experimental results, their numerical results do differ from those obtained with the M-integral. However, the present numerical results obtained by the M-integral agree well with those obtained by the three different methods used by Kim and Paulino [23] (see Table 13).

8. Concluding remarks

This paper develops the "non-equilibrium formulation" of the interaction integral method in conjunction with the FEM for evaluating the T-stress considering mixed-mode crack problems in two-dimensional FGMs. From numerical investigations, we observe that the T-stress computed by the present method is reasonably accurate in comparison with available reference solutions for mode I and mixed-mode prob-

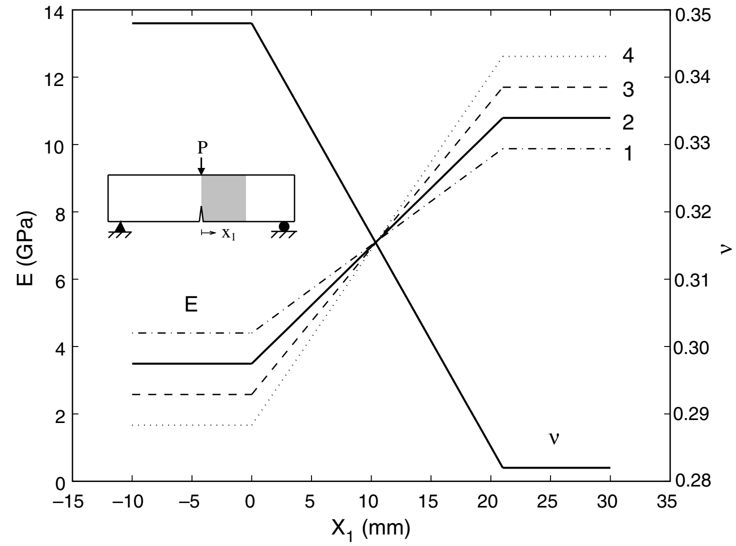

Fig. 31. Example 7: Variations of Young's modulus (E) and Poisson's ratio (ν) for Cases 1–4. The shaded portion in the insert indicates the graded material region and the solid lines in the graph indicate the material properties used by Marur and Tippur [74].

Table 11
Example 7: Variation of Young's modulus ($E(X_1)$) and Poisson's ratio ($\nu(X_1)$) for graded region of the beam illustrated by Fig. 30(a). Case 2 refers to the material properties used by Marur and Tippur [74]

Case	E (0 mm)	E (21 mm)	ν (0 mm)	ν (21 mm)
1	4.402 GPa	9.877 GPa	0.384	0.282
2	**3.490 GPa**	**10.790 GPa**	**0.384**	**0.282**
3	2.577 GPa	11.702 GPa	0.384	0.282
4	1.665 GPa	12.615 GPa	0.384	0.282

lems, and that material non-homogeneity influences the magnitude and the sign of the T-stress. The present numerical investigations for the T-stress and/or the biaxiality ratio presented here provide a guideline for fracture experiments on both monolithic (uniform composition) and FGM specimens (e.g. graded fracture laboratory specimens), and may complement fracture testing.

As observed in the boundary layer model study, the T-stress has larger domain dependence in non-homogeneous than in homogeneous materials (see Table 1). Moreover, we observe that the T-stress has larger domain dependence than the mode I SIF. For instance, for all the domains considered in the boundary layer model of Fig. 11, the T-stress varies within order $O(10^{-2})$ for homogeneous materials and $O(10^{-1})$ for non-homogeneous materials with $\gamma = 0.5$, while the mode I SIF changes within the order $O(10^{-4})$ for both materials (homogeneous and non-homogeneous). Such observation is consistent with the following statement in the manual of the commercial FEM software ABAQUS [75]: "In general, the T-stress has larger domain dependence or contour dependence than the J-integral and the stress intensity factors."

It may be noted that it is difficult to obtain accurate T-stress results. As motivated by Example 6, the accuracy of the T-stress can be improved with mesh refinement. In that example, a simple convergence study for T-stress is conducted through h-version refinement by increasing the number of sectors around the

Table 12
Example 7: T-stress and SIFs for three-point bending specimen with a crack perpendicular to material gradation (Case 1: $E = 4.402$ to 9.877 GPa; Case 2: $E = 3.490$ to 10.790 GPa; Case 3: $E = 2.577$ to 11.702 GPa; Case 4: $E = 1.665$ to 12.615 GPa)

E	Parameters	M-integral	Marur and Tippur [74]
Case 1	T	−1.042	–
	K_I	0.5711	–
	K_{II}	−0.0188	–
	$\lvert\mathbf{K}\rvert$	0.5714	–
	ψ	−1.88°	–
Case 2	T	−1.263	–
	K_I	0.5581	0.589
	K_{II}	−0.0277	−0.033
	$\lvert\mathbf{K}\rvert$	0.5587	0.59
	ψ	−2.84°	−3.24°
Case 3	T	−1.558	–
	K_I	0.5410	–
	K_{II}	−0.0390	–
	$\lvert\mathbf{K}\rvert$	0.5424	–
	ψ	−4.12°	–
Case 4	T	−1.996	–
	K_I	0.5176	–
	K_{II}	−0.0550	–
	$\lvert\mathbf{K}\rvert$	0.5205	–
	ψ	−6.06°	–

Table 13
Example 7: Comparison of SIFs for three-point bending specimen with crack perpendicular to material gradation (Case 2: $E = 3.490$ to 10.790 GPa)

Parameters	M-integral (present)	Kim and Paulino [23]			Marur and Tippur [74]	
		MCC	J_k^*-integral	DCT	FEM	Experiment
K_I	0.5581	0.557	0.557	0.558	0.589	0.6488
K_{II}	−0.0277	−0.028	−0.026	−0.026	−0.033	−0.0391
$\lvert\mathbf{K}\rvert$	0.5587	0.5575	0.5576	0.5580	0.59	0.65
ψ	−2.84°	−2.87°	−2.67°	−2.64°	−3.24°	−3.45°

crack-tip along the radial direction. Alternative approaches include improved numerical quadrature and p-version refinement [38]. Therefore, a natural extension for computing T-stress may be achieved by combining the present strategy with the p-version of Chen et al. [38] into a hp-version refinement.

Acknowledgements

We gratefully acknowledge the support from NASA-Ames, Engineering for Complex Systems Program, and the NASA-Ames Chief Engineer (Dr. Tina Panontin) through grant NAG 2-1424. We also acknowledge additional support from the National Science Foundation (NSF) under grant CMS-0115954 (Mechanics & Materials Program). In addition, we would like to thank three anonymous reviewers for their valuable comments and suggestions. Any opinions expressed herein are those of the writers and do not necessarily reflect the views of the sponsors.

Appendix A. Alternative formulations for *T*-stress

In fracture of FGMs, the use of the auxiliary fields developed for homogeneous materials results in violation of one of the three relations of mechanics: equilibrium, compatibility, and constitutive. The auxiliary fields chosen accounting for each of the violations lead to three independent formulations, i.e. non-equilibrium, incompatibility, and constant-constitutive-tensor formulations. For the sake of comparison with the non-equilibrium formulation addressed in this paper, the other two alternative formulations are derived below.

A.1. Incompatibility formulation

The incompatibility formulation satisfies equilibrium ($\sigma_{ij,j}^{\mathrm{aux}} = 0$ with no body forces) and the constitutive relationship ($\varepsilon_{ij}^{\mathrm{aux}} = S_{ijkl}(\boldsymbol{x})\sigma_{kl}^{\mathrm{aux}}$, where $S_{ijkl}(\boldsymbol{x})$ is the compliance tensor of FGMs), but violates compatibility conditions ($\varepsilon_{ij}^{\mathrm{aux}} \neq (u_{i,j}^{\mathrm{aux}} + u_{j,i}^{\mathrm{aux}})/2$). The expressions in Eqs. (22), (23), (25), and (26) are also valid for this formulation. Using equilibrium (actual and auxiliary) and compatibility (actual), one simplifies M_2 in Eq. (26) as

$$M_2 = \int_A \left\{ \sigma_{ij}(u_{i,1j}^{\mathrm{aux}} - \varepsilon_{ij,1}^{\mathrm{aux}}) - C_{ijkl,1}\varepsilon_{kl}\varepsilon_{ij}^{\mathrm{aux}} \right\} q \, \mathrm{d}A.$$

Therefore the resulting interaction integral (M) becomes

$$M = \int_A \left\{ \sigma_{ij}u_{i,1}^{\mathrm{aux}} + \sigma_{ij}^{\mathrm{aux}}u_{i,1} - \sigma_{ik}\varepsilon_{ik}^{\mathrm{aux}}\delta_{1j} \right\} q_{,j} \, \mathrm{d}A + \int_A \left\{ \underline{\sigma_{ij}(u_{i,1j}^{\mathrm{aux}} - \varepsilon_{ij,1}^{\mathrm{aux}})} - C_{ijkl,1}\varepsilon_{kl}\varepsilon_{ij}^{\mathrm{aux}} \right\} q \, \mathrm{d}A, \tag{A.1}$$

where the underlined term is an incompatible term, which appears due to incompatibility of the auxiliary strain fields. The incompatibility formulation for the extraction of mixed-mode stress SIFs in isotropic FGMs was first developed by Dolbow and Gosz [42]. It was also used by Rao and Rahman [76] (referred to as Method II in their paper) in conjunction with the element-free Galerkin (EFG) method.

A.2. Constant-constitutive-tensor formulation

The constant-constitutive-tensor formulation satisfies equilibrium ($\sigma_{ij,j}^{\mathrm{aux}} = 0$ with no body forces) and compatibility conditions ($\varepsilon_{ij}^{\mathrm{aux}} = (u_{i,j}^{\mathrm{aux}} + u_{j,i}^{\mathrm{aux}})/2$), but violates the constitutive relationship ($\sigma_{ij}^{\mathrm{aux}} = (C_{ijkl})_{\mathrm{tip}}\varepsilon_{kl}^{\mathrm{aux}}$ with $(C_{ijkl})_{\mathrm{tip}} \neq C_{ijkl}(\boldsymbol{x})$). Notice that $\sigma_{ij}\varepsilon_{ij}^{\mathrm{aux}} \neq \sigma_{ij}^{\mathrm{aux}}\varepsilon_{ij}$ due to violation of the constitutive relationship. Thus Eq. (22) becomes

$$\begin{aligned} M = &\int_A \left\{ \sigma_{ij}u_{i,1}^{\mathrm{aux}} + \sigma_{ij}^{\mathrm{aux}}u_{i,1} - \frac{1}{2}(\sigma_{ik}\varepsilon_{ik}^{\mathrm{aux}} + \sigma_{ik}^{\mathrm{aux}}\varepsilon_{ik})\delta_{1j} \right\} q_{,j} \, \mathrm{d}A + \int_A \left\{ \sigma_{ij,j}u_{i,1}^{\mathrm{aux}} + \sigma_{ij}u_{i,1j}^{\mathrm{aux}} + \sigma_{ij,j}^{\mathrm{aux}}u_{i,1} \right. \\ &\left. + \sigma_{ij}^{\mathrm{aux}}u_{i,1j} - \frac{1}{2}(\sigma_{ij,1}\varepsilon_{ij}^{\mathrm{aux}} + \sigma_{ij}\varepsilon_{ij,1}^{\mathrm{aux}} + \sigma_{ij,1}^{\mathrm{aux}}\varepsilon_{ij} + \sigma_{ij}^{\mathrm{aux}}\varepsilon_{ij,1}) \right\} q \, \mathrm{d}A. \end{aligned} \tag{A.2}$$

Using equilibrium and compatibility conditions for both actual and auxiliary fields, one obtains M as

$$\begin{aligned} M = &\int_A \left\{ \sigma_{ij}u_{i,1}^{\mathrm{aux}} + \sigma_{ij}^{\mathrm{aux}}u_{i,1} - \frac{1}{2}(\sigma_{ik}\varepsilon_{ik}^{\mathrm{aux}} + \sigma_{ik}^{\mathrm{aux}}\varepsilon_{ik})\delta_{1j} \right\} q_{,j} \, \mathrm{d}A \\ &+ \int_A \frac{1}{2} \left\{ \sigma_{ij}\varepsilon_{ij,1}^{\mathrm{aux}} - \sigma_{ij,1}\varepsilon_{ij}^{\mathrm{aux}} + \sigma_{ij}^{\mathrm{aux}}\varepsilon_{ij,1} - \sigma_{ij,1}^{\mathrm{aux}}\varepsilon_{ij} \right\} q \, \mathrm{d}A. \end{aligned} \tag{A.3}$$

Notice that the resulting M involves derivatives of the actual strain and stress fields, which arises due to the material mismatch, and may cause loss of accuracy from a numerical point of view. This formulation was discussed by Dolbow and Gosz [42], and it was presented and implemented by Rao and Rahman [76] (referred to as Method I in their paper) using a meshless method.

Appendix B. Nomenclature

a	half crack length
C_{ijkl} or $\mathbf{C}$	constitutive tensor; $i, j, k, l = 1, 2, 3$
d	the coordinate of a fixed point on the x_1 axis
e	natural logarithm base, $e = 2.71828182\ldots$
E	Young's modulus
E_{tip}	Young's modulus at the crack-tip
E_0	Young's modulus evaluated at the origin
E_1	Young's modulus at $X_1 = 0$ or $X_2 = 0$; $E_1 = E(0)$
E_2	Young's modulus at $X_1 = W$ or $X_2 = W$; $E_2 = E(W)$
F	point force applied to the crack-tip
$f_{ij}(\theta)$	angular function
$\mathscr{H}$	contour integral
J	path-independent J-integral for the actual field
J^{aux}	J-integral for the auxiliary field
J^{s}	J-integral for the superimposed fields (actual and auxiliary)
$\mathbf{J}$	Jacobian matrix
$\mathbf{J}^{-1}$	inverse of the Jacobian matrix
K_{I}	mode I stress intensity factor
K_{Ic}	fracture toughness
K_{II}	mode II stress intensity factor
$\lvert\mathbf{K}\rvert$	norm of stress intensity factors, $\lvert\mathbf{K}\rvert = \sqrt{K_{\mathrm{I}}^2 + K_{\mathrm{II}}^2}$
L	length of a plate
M	interaction integral (M-integral)
m_i, n_i	unit normal vectors on the contour of the domain integral
N_i	shape function for node i of the element; $N_i = N_i(\xi, \eta)$
P	point force or load resultant
q	weight function in the domain integral
r	radial direction in polar coordinates
R	radius of a disk
r_{c}	fracture process zone size
S_{ijkl} or $\mathbf{S}$	compliance tensor for anisotropic materials; $i, j, k, l = 1, 2, 3$
T	T-stress
t	thickness of specimens
u_i	displacements for the actual field; $i = 1, 2$
u_i^{aux}	displacements for the auxiliary field; $i = 1, 2$
$u_{i,j}$	displacement derivatives for the actual field; $i, j = 1, 2$
$u_{i,j}^{\mathrm{aux}}$	displacement derivatives for the auxiliary field; $i, j = 1, 2$
W	width of a plate
$\mathscr{W}$	strain energy density

$\mathscr{W}^{aux}$	strain energy density for the auxiliary field
x_i	local Cartesian coordinates; $i = 1, 2$
X_i	global Cartesian coordinates; $i = 1, 2$
α	crack geometry angle
α_p	proportionality factor
β	biaxiality ratio; $\beta = T\sqrt{\pi a}/K_I$
γ	material non-homogeneity parameter
Γ	contour for J and M integrals
Γ_0	outer contour
Γ_s	inner contour
Γ^+	contour along the upper crack face
Γ^-	contour along the lower crack face
δ_{ij}	Kronecker delta; $i, j = 1, 2$
λ	a load factor for σ_{11}
ε_{ij}	strains for the actual fields; $i, j = 1, 2$
ε_{ij}^{aux}	strains for the auxiliary fields; $i, j = 1, 2$
θ	angular direction in polar coordinates
κ	material parameter, $\kappa = (3 - v)/(1 + v)$ for plane stress and $\kappa = 3 - 4v$ for plane strain
κ_{tip}	κ evaluated at the crack-tip
μ	shear modulus
μ_{tip}	shear modulus evaluated at the crack-tip
v	Poisson's ratio
v_{tip}	Poisson's ratio at the crack-tip
ψ	phase angle; $\psi = \tan^{-1}(K_{II}/K_I)$
σ_{ij}	stresses for the actual fields; $i, j = 1, 2$
σ_{ij}^{aux}	stresses for the auxiliary fields; $i, j = 1, 2$
σ_Y	yield stress
ω	a/R for internal crack and $a/2R$ for an edge crack

References

[1] Hirai T. Functionally gradient materials and nanocomposites. In: Holt JB, Koizumi M, Hirai T, Munir ZA, editors. Proceedings of the Second International Symposium on Functionally Gradient Materials. Ceramic Transactions, vol. 34. Westerville, Ohio: The American Ceramic Society; 1993. p. 11–20.

[2] Ilschner B. Processing-microstructure-property relationships in graded materials. J Mech Phys Solids 1996;44(5):647–56.

[3] Suresh S, Mortensen A. Fundamentals of functionally graded materials. London: IOM Communications Ltd; 1998.

[4] Miyamoto Y, Kaysser WA, Rabin BH, Kawasaki A, Ford RG. Functionally graded materials: design, processing and applications. Dordrecht: Kluwer Academic Publishers; 1999.

[5] Paulino GH, Jin ZH, Dodds Jr RH. Failure of functionally graded materials. In: Karihaloo B, Knauss WG, editors. Comprehensive structural integrity, vol. 2. Elsevier Science; 2003. p. 607–44 [chapter 13].

[6] Hirano T, Teraki J, Yamada T. On the design of functionally gradient materials. In: Yamanouochi M, Koizumi M, Hirai T, Shiota I, editors. Proceedings of the First International Symposium on Functionally Gradient Materials, Sendai, Japan, 1990. p. 5–10.

[7] Igari T, Notomi A, Tsunoda H, Hida K, Kotoh T, Kunishima S. Material properties of functionally gradient material for fast breeder reactor. In: Yamanouochi M, Koizumi M, Hirai T, Shiota I, editors. Proceedings of the First International Symposium on Functionally Gradient Materials, Sendai, Japan, 1990. p. 209–14.

[8] Tani J, Liu GR. SH surface waves in functionally gradient piezoelectric plates. JSME Int J Ser A (Mech Mater Engng) 1993;36(2):152–5.

[9] Hirano T, Whitlow LW, Miyajima M. Numerical analysis of efficiency improvement in functionally gradient thermoelectric materials. In: Holt JB, Koizumi M, Hirai T, Munir ZA, editors. Proceedings of the Second International Symposium on Functionally Gradient Materials. Ceramic Transactions, vol. 34. Westerville, Ohio: The American Ceramic Society; 1993. p. 23–30.

[10] Osaka T, Matsubara H, Homma T, Mitamura S, Noda K. Microstructural study of electroless-plated CoNiReP/NiMoP double-layered media for perpendicular magnetic recording. Jpn J Appl Phys 1990;29(10):1939–43.

[11] Watanabe Y, Nakamura Y, Fukui Y, Nakanishi K. A magnetic-functionally graded material manufactured with deformation-induced martensitic transformation. J Mater Sci Lett 1993;12(5):326–8.

[12] Koike Y. Graded-index and single mode polymer optical fibers. In: Chiang LY, Garito AG, Sandman DJ, editors. Electrical, optical, and magnetic properties of organic solid state materials, vol. 247. Materials Research Society Proceedings, Pittsburgh, PA, 1992. p. 817.

[13] Desplat JL. Recent development on oxygenated thermionic energy converter—overview. In: Proceedings of the Fourth International Symposium on Functionally Gradient Materials, Tsukuba City, Japan, 1996.

[14] Watari F, Yokoyama A, Saso F, Uo M, Ohkawa S, Kawasaki T. EPMA elemental mapping of functionally graded dental implant in biocompatibility test. In: Proceedings of the Fourth International Symposium on Functionally Gradient Materials, Tsukuba City, Japan, 1996.

[15] Oonishi H, Noda T, Ito S, Kohda A, Yamamoto H, Tsuji E. Effect of hydroxyapatite coating on bone growth into porous titanium alloy implants under loaded conditions. J Appl Biomater 1994;5(1):23–7.

[16] Getto H, Ishihara SJ. Development of the fire retardant door with functional gradient wood. In: Proceedings of the Fourth International Symposium on Functionally Gradient Materials, Tsukuba City, Japan, 1996.

[17] Eischen JW. Fracture of non-homogeneous materials. Int J Fract 1987;34(1):3–22.

[18] Williams ML. On the stress distribution at the base of a stationary crack. J Appl Mech, Trans ASME 1957;24(1):109–14.

[19] Eftis J, Subramonian N, Liebowitz H. Crack border stress and displacement equations revisited. Engng Fract Mech 1977;9(1):189–210.

[20] Anderson TL. Fracture mechanics: fundamentals and applications. Boca Raton: CRC Press LLC; 1995.

[21] Irwin G. Analysis of stresses and strains near the end of a crack traversing a plate. J Appl Mech, Trans ASME 1957;24: 361–4.

[22] Gu P, Asaro RJ. Crack deflection in functionally graded materials. Int J Solids Struct 1997;34(24):3085–98.

[23] Kim J-H, Paulino GH. Finite element evaluation of mixed-mode stress intensity factors in functionally graded materials. Int J Numer Meth Engng 2002;53(8):1903–35.

[24] Leevers PS, Radon JC. Inherent stress biaxiality in various fracture specimen geometries. Int J Fract 1982;19(4):311–25.

[25] Du Z-Z, Hancock JW. The effect of non-singular stresses on crack-tip constraint. J Mech Phys Solids 1991;39(3):555–67.

[26] Larsson SG, Carlson AJ. Influence of non-singular stress terms and specimen geometry on small-scale yielding at crack-tips in elastic–plastic materials. J Mech Phys Solids 1973;21(4):263–77.

[27] O'Dowd NP, Shih CF, Dodds Jr RH. The role of geometry and crack growth on constraint and implications for ductile/brittle fracture. In: Constraint effects in fracture theory and applications. ASTM STP 1244, vol. 2. American Society for Testing and Materials; 1995. p. 134–59.

[28] Williams JG, Ewing PD. Fracture under complex stress—the angled crack problem. Int J Fract 1972;8(4):416–41.

[29] Ueda Y, Ikeda K, Yao T, Aoki M. Characteristics of brittle failure under general combined modes including those under bi-axial tensile loads. Engng Fract Mech 1983;18(6):1131–58.

[30] Kim J-H, Paulino GH. *T*-stress, mixed-mode stress intensity factors, and crack initiation angles in functionally graded materials: a unified approach using the interaction integral method. Comput Meth Appl Mech Engng 2003;192(11–12):1463–94.

[31] Smith DJ, Ayatollahi MR, Pavier MJ. The role of *T*-stress in brittle fracture for linear elastic materials under mixed-mode loading. Fatigue Fract Engng Mater Struct 2001;24(2):137–50.

[32] Cotterell B, Rice JR. Slightly curved or kinked cracks. Int J Fract 1980;16(2):155–69.

[33] Melin S. The influence of the *T*-stress on the directional stability of cracks. Int J Fract 2002;114(3):259–65.

[34] Cardew GE, Goldthorpe MR, Howard IC, Kfouri AP. On the elastic *T*-term. In: Fundamentals of Deformation and Fracture: Eshelby Memorial Symposium, 1985.

[35] Kfouri AP. Some evaluations of the elastic *T*-term using Eshelby's method. Int J Fract 1986;30(4):301–15.

[36] Sherry AH, France CC, Goldthorpe MR. Compendium of *T*-stress solutions for two and three dimensional cracked geometries. Fatigue Fract Engng Mater Struct 1995;18(1):141–55.

[37] Sladek J, Sladek V, Fedelinski P. Contour integrals for mixed-mode crack analysis: effect of nonsingular terms. Theor Appl Fract Mech 1997;27(2):115–27.

[38] Chen CS, Krause R, Pettit RG, Banks-Sills L, Ingraffea AR. Numerical assessment of *T*-stress computation using a *p*-version finite element method. Int J Fract 2001;107(2):177–99.

[39] Carrillo-Heian EM, Carpenter RD, Paulino GH, Gibeling JC, Munir ZA. Dense layered molybdenum disilicide-silicon carbide functionally graded composites formed by field-activated synthesis. J Amer Ceram Soc 2001;84(5):962–8.

[40] Becker Jr TL, Cannon RM, Ritchie RO. Finite crack kinking and T-stresses in functionally graded materials. Int J Solids Struct 2001;38(32–33):5545–63.
[41] Michell JH. Elementary distributions of plane stress. Proc Lond Math Soc 1900;32:35–61.
[42] Dolbow J, Gosz M. On the computation of mixed-mode stress intensity factors in functionally graded materials. Int J Solids Struct 2002;39(9):2557–74.
[43] Knowles JK, Sternberg E. On a class of conservation laws in linearized and finite elastostatics. Arch Ration Mech Anal 1972;44(2):187–211.
[44] Budiansky B, Rice JR. Conservation laws and energy-release rates. J Appl Mech, Trans ASME 1973;40(1):201–3.
[45] Chang JH, Chien AJ. Evaluation of M-integral for anisotropic elastic media with multiple defects. Int J Fract 2002;114(3):267–89.
[46] Kanninen MF, Popelar CH. Advanced fracture mechanics. New York: Oxford University Press; 1985.
[47] Rice JR. A path-independent integral and the approximate analysis of strain concentration by notches and cracks. J Appl Mech, Trans ASME 1968;35(2):379–86.
[48] Nikishkov GP, Atluri SN. Calculation of fracture mechanics parameters for an arbitrary three-dimensional crack by the 'equivalent domain integral' method. Int J Numer Meth Engng 1987;24:1801–21.
[49] Anlas G, Santare MH, Lambros J. Numerical calculation of stress intensity factors in functionally graded materials. Int J Fract 2000;104(2):131–43.
[50] Kim J-H, Paulino GH. Mixed-mode J-integral formulation and implementation using graded finite elements for fracture analysis of nonhomogeneous orthotropic materials. Mech Mater 2003;35(1–2):107–28.
[51] Erdogan F. Fracture mechanics of functionally graded materials. Compos Engng 1995;5(7):753–70.
[52] Delale F, Erdogan F. The crack problem for a nonhomogeneous plane. J Appl Mech, Trans ASME 1983;50(3):609–14.
[53] Erdogan F, Wu BH. The surface crack problem for a plate with functionally graded properties. J Appl Mech, Trans ASME 1997;64(3):449–56.
[54] Chan Y-S, Paulino GH, Fannjiang AC. The crack problem for nonhomogeneous materials under antiplane shear loading—a displacement based formulation. Int J Solids Struct 2001;38(17):2989–3005.
[55] Delale F, Erdogan F. On the mechanical modeling of an interfacial region in bonded half-planes. J Appl Mech, Trans ASME 1988;55(2):317–24.
[56] Gu P, Asaro RJ. Cracks in functionally graded materials. Int J Solids Struct 1997;34(1):1–17.
[57] Shbeeb NI, Binienda WK, Kreider KL. Analysis of the driving forces for multiple cracks in an infinite nonhomogeneous plate, Part I: Theoretical analysis. J Appl Mech, Trans ASME 1999;66(2):492–500.
[58] Shbeeb NI, Binienda WK, Kreider KL. Analysis of the driving forces for multiple cracks in an infinite nonhomogeneous plate, Part II: Numerical solutions. J Appl Mech, Trans ASME 1999;66(2):501–6.
[59] Honein T, Herrmann G. Conservation laws in nonhomogeneous plane elastostatics. J Mech Phys Solids 1997;45(5):789–805.
[60] Ozturk M, Erdogan F. Mode I crack problem in an inhomogeneous orthotropic medium. Int J Engng Sci 1997;35(9):869–83.
[61] Ozturk M, Erdogan F. The mixed mode crack problem in an inhomogeneous orthotropic medium. Int J Fract 1999;98(3–4):243–61.
[62] Kim J-H, Paulino GH. Isoparametric graded finite elements for nonhomogeneous isotropic and orthotropic materials. J Appl Mech, Trans ASME 2002;69(4):502–14.
[63] Santare MH, Lambros J. Use of graded finite elements to model the behavior of nonhomogeneous materials. J Appl Mech, Trans ASME 2000;67(4):819–22.
[64] Konda N, Erdogan F. The mixed mode crack problem in a nonhomogeneous elastic medium. Engng Fract Mech 1994;47(4):533–45.
[65] Paulino GH, Dong Z. A novel application of the singular integral equation approach to evaluate T-stress in functionally graded materials (in preparation).
[66] Cook RD, Malkus DS, Plesha ME, Witt RJ. Concepts and applications of finite element analysis. 4th ed. New York: John Wiley & Sons, Inc; 2001.
[67] Wawrzynek PA. Interactive finite element analysis of fracture processes: an integrated approach. MS Thesis, Cornell University, 1987.
[68] Wawrzynek PA, Ingraffea AR. Discrete modeling of crack propagation: theoretical aspects and implementation issues in two and three dimensions. Report 91-5, School of Civil Engineering and Environmental Engineering, Cornell University, 1991.
[69] Marur PR, Tippur HV. Evaluation of mechanical properties of functionally graded materials. J Test Eval 1998;26(6):539–45.
[70] Kim J-H. Mixed-mode crack propagation in functionally graded materials. PhD Thesis, University of Illinois at Urbana-Champaign, 2003.
[71] Fett T. T-stresses in rectangular plates and circular disks. Engng Fract Mech 1998;60(5–6):631–52.
[72] Fett T. Stress intensity factors and T-stress for internally cracked circular disks under various boundary conditions. Engng Fract Mech 2001;68(9):1119–36.
[73] Fett T. Stress intensity factors and T-stress for single and double-edge-cracked circular disks under mixed boundary conditions. Engng Fract Mech 2002;69(1):69–83.

[74] Marur PR, Tippur HV. Numerical analysis of crack-tip fields in functionally graded materials with a crack normal to the elastic gradient. Int J Solids Struct 2000;37(38):5353–70.
[75] Hibbitt, Karlson, & Sorensen. ABAQUS/Standard user's manual, Version 6.2, vol. I. Pawtucket, RI: Hibbitt, Karlson & Sorensen, Inc; 2000. p. 7.8.2–6.
[76] Rao BN, Rahman S. Mesh-free analysis of cracks in isotropic functionally graded materials. Engng Fract Mech 2003;70(1):1–27.